The Innovation

Article

Subtle Side Chain Triggers Unexpected Two-Channel Charge Transport Property Enabling 80% Fill Factors and Efficient Thick-Film Organic Photovoltaics

Yonghai Li,[1,3,*] Lu Yu,[1,2] Liangliang Chen,[4] Chenyu Han,[1] Huanxiang Jiang,[1] Zitong Liu,[4] Nan Zheng,[5,*] Jiuxing Wang,[6] Mingliang Sun,[2] Renqiang Yang,[1,7,*] and Xichang Bao[1,3,*]

*Correspondence: liyh@qibebt.ac.cn (Y.L.); zhengn@scut.edu.cn (N.Z.); yangrq@qibebt.ac.cn (R.Y.); baoxc@qibebt.ac.cn (X.B.)

Received: November 6, 2020; Accepted: February 1, 2021; Published Online: February 4, 2021; https://doi.org/10.1016/j.xinn.2021.100090

GRAPHICAL ABSTRACT

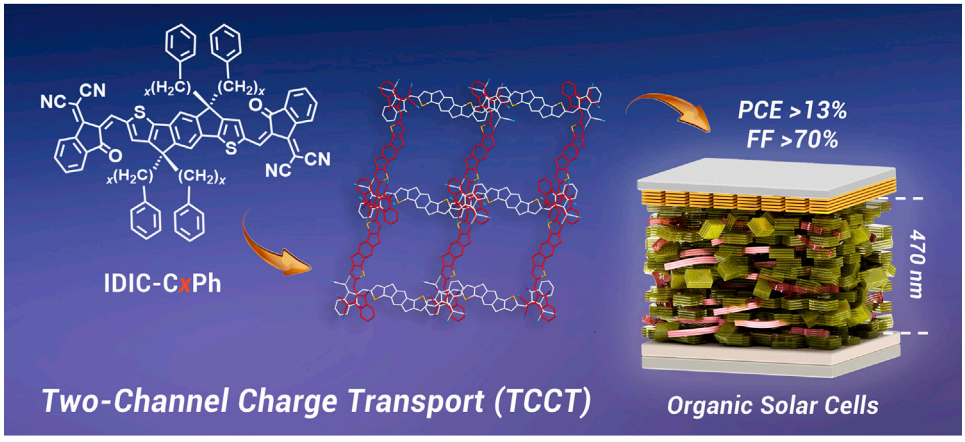

PUBLIC SUMMARY

- OSCs are a promising technology to transform the solar energy to electricity
- This article reports an efficient TCCT photovoltaic material through subtle side-chain modification
- The TCCT property enables 13% efficiency with FF reaching 70% in 470 nm thick-film photovoltaics

Article

Subtle Side Chain Triggers Unexpected Two-Channel Charge Transport Property Enabling 80% Fill Factors and Efficient Thick-Film Organic Photovoltaics

Yonghai Li,[1,3,*] Lu Yu,[1,2] Liangliang Chen,[4] Chenyu Han,[1] Huanxiang Jiang,[1] Zitong Liu,[4] Nan Zheng,[5,*] Jiuxing Wang,[6] Mingliang Sun,[2] Renqiang Yang,[1,7,*] and Xichang Bao[1,3,*]

[1]CAS Key Laboratory of Bio-based Materials, Qingdao Institute of Bioenergy and Bioprocess Technology, Chinese Academy of Sciences, Qingdao 266101, China

[2]School of Material Science and Engineering, Ocean University of China, Qingdao 266100, China

[3]Functional Laboratory of Solar Energy, Shandong Energy Institute, Qingdao 266101, China

[4]Beijing National Laboratory for Molecular Sciences, CAS Key Laboratory of Organic Solids, Institute of Chemistry, Chinese Academy of Sciences, Beijing 100190, China

[5]State Key Laboratory of Luminescent Materials and Devices, South China University of Technology, Guangzhou 510640, China

[6]School of Materials Science and Engineering, Qingdao University, Qingdao 266071, China

[7]Key Laboratory of Optoelectronic Chemical Materials and Devices (Ministry of Education), School of Chemical and Environmental Engineering, Jianghan University, Wuhan 430056, China

*Correspondence: liyh@qibebt.ac.cn (Y.L.); zhengn@scut.edu.cn (N.Z.); yangrq@qibebt.ac.cn (R.Y.); baoxc@qibebt.ac.cn (X.B.)

Received: November 6, 2020; Accepted: February 1, 2021; Published Online: February 4, 2021; https://doi.org/10.1016/j.xinn.2021.100090

Citation: Li Y., Yu L., Chen L., et al., (2021). Subtle Side Chain Triggers Unexpected Two-Channel Charge Transport Property Enabling 80% Fill Factors and Efficient Thick-Film Organic Photovoltaics. The Innovation **2(1)**, 100090.

To clearly show how important the impact of side chains on organic solar cells (OSCs) is, we designed three acceptors IDIC-CxPh (*x* = 4, 5, or 6) via subtle side-chain regulation. Despite this small change, significant distinctions were detected. IDIC-C4Ph devices achieve an optimal efficiency of 13.94% under thermal annealing, but thermal-assistant solvent-vapor annealing hugely suppresses the efficiencies to 10%. However, the C6Ph side chain endows extremely disordered stacking orientations, generating moderate efficiencies of ~12.50%. Excitingly, the IDIC-C5Ph affords an unexpected two-channel π-π charge transport (TCCT) property, boosting the fill factor (FF) by up to 80.02% and efficiency to 14.56%, ranking the best among five-ring fused-ladder-type acceptors. Impressively, the special TCCT behavior of IDIC-C5Ph enables 470 nm thick-film OSC with a high FF of up to 70.12% and efficiency of 13.01%, demonstrating the great promise in fabricating large-scale OSCs.

KEYWORDS: organic solar cells; side chain; molecular assembly; two-channel charge transport; thick-film

INTRODUCTION

Organic solar cells (OSCs) have been recognized as a promising technology to efficiently harvest solar energy because of its light-weight, low-cost, and printable potential.[1–3] Excitingly, since 2015, the power conversion efficiencies (PCEs) have been greatly improved by small-molecule acceptors.[4,5] Benefiting from the acceptor Y6 and its derivatives, PCEs of over 17% have been recorded, signifying bright applications for OSCs.[6–12]

It is well established that photovoltaic performance is significantly influenced by nanoscale morphologies of bulk heterojunction (BHJ) blends.[13] A preferred BHJ usually involves nanoscale phase-separated interpenetrating networks and well-organized molecular stacking, which facilitates exciton dissociation and balances the hole/electron carrier transport, and finally improves the photovoltaic parameters, particularly short-circuit current densities (J_{SC}) and fill factors (FFs). More importantly, high-quality BHJ microstructures and advantageous charge transport properties could improve the tolerance of efficiency to active layer film thickness, which is one prerequisite for large-scale device fabrication. With regard to materials, crystallinity or aggregation property play critical roles in controlling BHJ morphologies. Intensive reports have revealed that the increased crystallinity of polymeric or small-molecule donors could improve BHJ morphologies and generate greater PCEs.[14–18] Likewise, considerable efforts have been dedicated to the regulation of crystallinity of nonfullerene acceptors.[19–22] In addition to the π-conjugated molecular backbones, side-chain engineering has been recognized as one facile efficient approach to regulate material crystallinity and BHJ microstructures to provide solubilities for solution processing of active layers.[23,24]

With regard to the influential ladder-type nonfullerene acceptors that have emerged since 2015, we note that nearly all reports focused on the crystallinity enhancement for higher efficiency. This is mainly ascribed to the widely used aryl-type side chains, which afford inherent insufficient crystallinity by way of the bulky steric hindrance close to the π backbone, and further leads to lower electron mobilities, blue-shifted absorption, and smaller extinction coefficients than the well-aligned n-alkyl side-chain-attached analogs.[25–27] As for Y6 structural acceptors, which feature long and branched alkyl side chains at the large π backbones, adjustment of these side chains is also essential to achieve a better crystallinity and more preferred BHJ properties.[6,28–30] Different from these discoveries, we present a fresh perspective to modulate the BHJ morphologies by attachment of a simple bulky phenyl at the alkyl chain terminal (IDIC-C4Ph), which moderately lowers the crystallinity of the acceptor, suppresses the excessive self-aggregation, and benefits the formation of fine nanoscale morphologies.[31] Interestingly, solar cells with high crystalline alkyl side-chain-modified IDIC recorded best efficiency at ~12% with FFs ~70% from as-cast devices, and post-treatments inevitably reduced the performance.[31,32] On the contrary, IDIC-C4Ph-based devices delivered much higher PCEs of ~14% with enhanced FFs to 78% under thermal annealing (TA) optimization.[31] Therefore, we believe that this type of alkyl chain-phenyl terminal has a fascinating impact on the material crystallinity and photovoltaic performance, and could probably afford some new interesting findings with regard to the structure-function relationship.

To further confirm great the impact of side chains, here we systematically investigated the subtle alkyl chain from n-C_4H_8- to n-C_6H_{12}-, which are inserted between the backbone and phenyl terminal and three acceptors IDIC-CxPh (*x* = 4, 5, 6) (Figure 1). Despite this very small change, significantly different crystallinity and molecular stacking in both crystals and films were noted. Compared with IDIC-C4Ph, which has higher crystallinity and face-on orientation, the crystallinity of IDIC-C5Ph and IDIC-C6Ph is weakened, and the oriented face-on orientation tends to be disordered in IDIC-C6Ph. These variations result in different BHJ morphologies and photovoltaic performance. The stronger crystalline IDIC-C4Ph-based OSCs generate an optimal PCE of 13.94% under TA conditions, but thermal-assistant solvent-vapor

Article

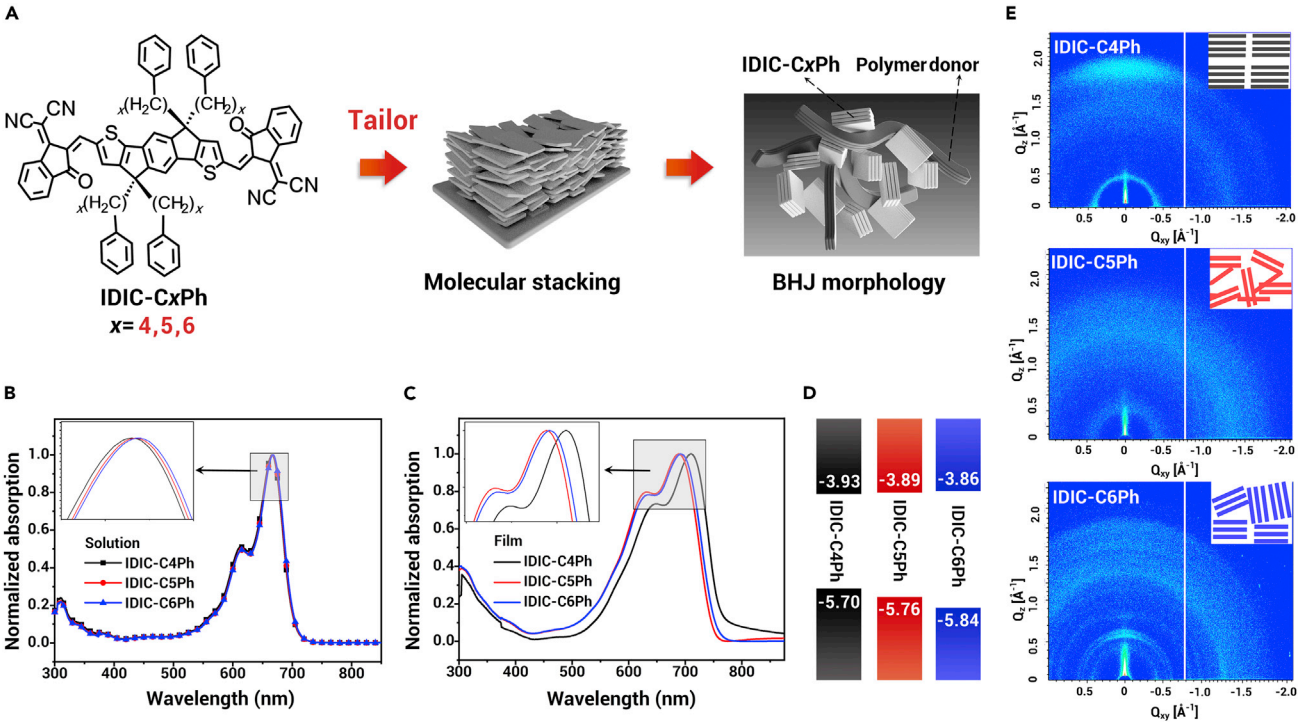

Figure 1. Basic Properties of Acceptors (A) Molecular structures and research approach. (B and C) Absorption spectra in chloroform solutions and thin films. (D) Energy level diagrams. (E) GIWAXS scattering patterns of the three acceptors. The insets show the arrangement sketch map of molecules in films.

annealing (TA-SVA) destroys the nanoscale networks and produces significantly reduced PCEs of ~10% with FFs <65%. The extremely disordered orientations of IDIC-C6Ph produce ungovernable BHJ morphologies, delivering a modest PCE of 12.57% after optimizations. On the contrary, equally moderate PCEs of ~12.50% with FFs of ~72% are achieved from IDIC-C5Ph-based as-cast and TA devices. Unexpectedly, IDIC-C5Ph affords efficient two-channel π-π charge transport (TCCT) properties in crystal and TA-SVA optimized films. This special charge transport channel enables BHJs with dramatically improved nanoscale phase separation with stronger and more balanced charge transport behaviors, leading to a remarkably increased PCE of up to 14.56%, contributed by the excellent FFs of up to 80.02%. Notably, the observation of this special TCCT property of IDIC-C5Ph again verifies the great importance of side chains in controlling the charge transport behaviors of organic optoelectronic materials. Encouraged by the TCCT properties and high FFs of IDIC-C5Ph-based solar cells, we fabricated thick-film active layer devices, which demonstrate good insensitive dependence on thickness. Devices of 470 nm thickness can still give a high FF of over 70% with a PCE over 13%, suggesting the bright promise in fabrication of large-scale OSCs.

RESULTS AND DISCUSSION

The synthetic details of the three acceptors are collected in Scheme S1. Different from the conventional alkyl side chains, all the side chains of IDIC-CxPh (x = 4, 5, or 6) terminate with phenyl groups, which are attached from the n-alkyl bromide and incorporated to the IDT core. Thermogravimetric analysis plots verify the good thermal stability with decomposition temperatures (T_d, 5% weight loss) of above 310°C (Figure S1). The highest occupied molecular orbital and lowest unoccupied molecular orbital energy levels are evaluated from cyclic voltammetry (Figure S2), and negligible variations are afforded by these subtly changed non-conjugated side chains. UV-vis absorption spectra in dilute solutions are shown in Figure 1B. It seems that the solution absorption profiles of the three acceptors remain almost overlapped. However, we can still distinguish that the maximum peaks gradually red shift by ~1 nm when increasing one methylene in CxPh, suggesting very slightly different intermolecular interactions. This small distinction is probably correlated with the remaining inter-chain interactions, because the π-π stacking is insignificant in dilute solutions. The differences in films are further enlarged, as shown in Figure 1C. The film absorption spectrum of IDIC-C4Ph receives obvious red shifts by 22 and 18 nm (maximum peak) compared with IDIC-C5Ph and IDIC-C6Ph, respectively. This probably means that, with the extension of CxPh, the solid molecular stacking is inevitably disturbed. These offsets induce varied optical band gaps for IDIC-C4Ph (1.62 eV), IDIC-C5Ph (1.66 eV), and IDIC-C6Ph (1.65 eV). Abstrusely, we noted that the absorption of the IDIC-C5Ph film is blue shifted by 4 nm than that of IDIC-C6Ph.

To understand the incomprehensible absorption offsets in films, we performed grazing incidence wide-angle X-ray scattering (GIWAXS) measurements and the results are shown in Figures 1E and S3. The preparation of GIWAXS samples are exactly the same as their absorption samples. As indicated in Figure 1E, a clearly observable π-π stacking diffraction spot at Q_Z = 1.84 Å in out-of-plane (OOP) is detected in IDIC-C4Ph, signifying good crystallization and a well-organized face-on orientation.[33,34] Besides, the ratio of π-π diffractions in OOP and in-plane (IP) directions are roughly calculated to be 7.5:1 for IDIC-C4Ph, suggesting the dominant face-on stacking orientation favored by OSCs with oriented vertical charge transport. On the contrary, series of weak diffraction rings are observed from IDIC-C6Ph patterns, indicating an intrinsic weaker crystallinity and disordered orientations.[35] Nevertheless, many weak diffraction peaks can be detected from both the OOP and IP directions (Figure S3). However, the IDIC-C5Ph film lacks any identifiable diffraction plots or rings. This suggests the weakest crystallinity of IDIC-C5Ph among the three acceptors, and partly explains the slightly blue-shifted absorption than IDIC-C6Ph. To further confirm this minor difference, we performed differential scanning calorimetry measurements and the curves are shown in Figures S4–S6. IDIC-C5Ph displays a sharp endothermic peak at 243°C (64.72 J g^{-1}) during the heating process and no exothermic peaks during the cooling process. While, for IDIC-C6Ph, an exothermic crystallinity process (186°C, −44.6 J g^{-1}) is detected during the cooling process. This again verifies the higher crystallinity of IDIC-C6Ph than IDIC-C5Ph. Considering the crystallinity, it seems that the IDIC-C5Ph with the lowest crystallinity would produce the least attractive photovoltaic property, as judged from many previous reports.[15–17]

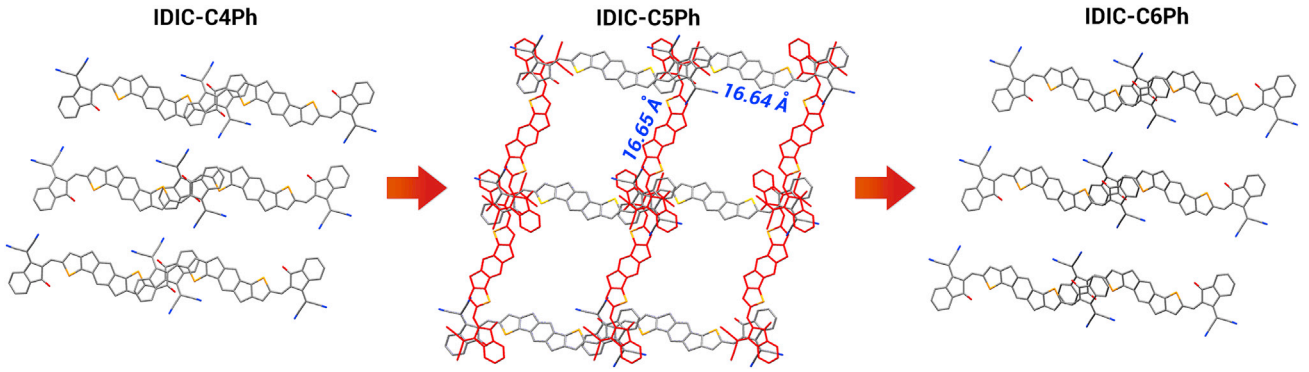

Figure 2. Single-Crystal Studies The molecular packing of three acceptors in single crystals.

To explore the molecular stacking of acceptors more intuitively, we cultured their single crystals and obtained their molecule packing modes using X-ray crystallography.[36] The crystallography data are collected in Tables S1–S3. Figure 2 displays the packing modes with the CxPh side chains hidden for a clear comparison. The detailed molecular packing with side chains is shown in Figures S7–S9, which indicates that all the side chains are nearly perpendicular to the molecular backbones. However, the assembly of the backbones differs significantly. Both IDIC-C4Ph and IDIC-C6Ph pack in a similar dislocation parallel mode. Amazingly, there are two types of stacking orientations in the IDIC-C5Ph crystal, with the main backbones almost orthogonal. Distinctively, the IDIC-C5Ph molecules form regular diamond structures with side lengths of ~16.65 Å. As a result, a more compact IDIC-C5Ph molecular assembly with multidimensional intermolecular π-π stacking emerges, including the horizontal and vertical axis molecular backbones and the two molecules adjacent to the axes. Notably, this interesting molecular assembly could produce two orthogonal π-π channels for faster charge transport, which we name the TCCT model. We noted that the densities calculated from single crystals are also different. The density of IDIC-C5Ph is determined to be 1.253 g cm^{-3}, higher than both IDIC-C4Ph (1.199 g cm^{-3}) and IDIC-C6Ph (1.194 g cm^{-3}), which also indicates a tighter intermolecular stacking of IDIC-C5Ph. To further verify this special molecular assembly, we conducted density functional theory quantum-mechanical calculations, which are shown in Figure S10. The results confirm the existence of two different molecular orientations of IDIC-C5Ph and are well consistent with the crystals. Apparently, the molecular stacking in crystals is different from that inferred from the GIWAXS patterns, which is induced by the differential molecular assembly in crystals and films. Yet, inspiringly, if we could effectively improve the film crystallinity of IDIC-C5Ph, it probably would afford similar TCCT crystal properties, giving significantly enhanced charge transport behaviors.

To evaluate the photovoltaic properties, we prepared OSCs with a conventional structure of ITO/PEDOT:PSS/PBDB-TF:acceptor/PDINO/Al. The chemical structure of PBDB-TF is shown in Figure S11. The photovoltaic parameters with different PBDB-TF:acceptor weight ratios are collected in Table S4. The representative results based on over 40 cells are shown in Table 1 and Figure 3. We noted that, for the three as-cast devices, IDIC-C4Ph generates the best PCE of 13.20% with FF of 76.77%. However, decreased PCEs are observed from IDIC-C5Ph devices with a lower PCE of 12.52% and FF of 71.37%. Disappointingly, the IDIC-C6Ph devices display the lowest PCE of 10.14% and inferior FF of 66.68%. Then, we conducted TA and TA-SVA post-treatments to optimize the OSCs; the processing details are described in the Supplemental information. The TA-treated IDIC-C4Ph OSC reaches its optimal PCE of 13.94% with a high FF of 78.05%. However, TA-SVA causes sharply reduced PCEs of ~10% with poor FFs of ~62%. These significantly changed parameters usually correlate with a drastic degeneration of BHJ morphology, as discussed below. For IDIC-C5Ph-based devices, minor improvement is recorded after TA. However, it is surprising that TA-SVA enables strikingly boosted PCEs of up to 14.56%, attributed to the hugely enhanced FF of up to 80.02%. Also, the high average PCE and small variance (14.34% ± 0.20%) emphasizes the good repeatability of TA-SVA to IDIC-C5Ph cells. For IDIC-C6Ph-based devices, TA mildly improves the PCE to 11.52%. After TA-SVA, some desirable FFs of over 76% but still low J_{SC} values are achieved, contributing to a PCE of 12.54%. However, the disappointing repeatability of TA-SVA-treated IDIC-C6Ph devices is noted. Low average PCEs with a large variance (11.72% ± 0.90%) are obtained, with erratic FFs (73.90% ± 2.75%) being responsible. We infer that the inferior PCEs and repeatability of IDIC-C6Ph devices are probably because of the tough-to-optimized BHJ morphologies, which are correlated with the disordered stacking orientations of IDIC-C6Ph molecules. Besides, it seems that the best post-process approach in IDIC-C*x*Ph (*x* = 4, 5, or 6) system is closely related to the crystallinity and molecular packing tailored by the subtle change in the side chain. Mild TA treatment is useful for IDIC-C4Ph with preferred crystallinity and orientation. The increased side chain to C5Ph lowered the crystallinity, requiring TA-SVA to build the preferred BHJ microstructures. However, optimizing the performance of IDIC-C6Ph with the usual post-treatments is difficult. These results suggest that this inconspicuous side-chain modification not only significantly influenced the photovoltaic performance, but also altered their optimal post-process approaches.

Typically, it is worth highlighting that all three OSCs deliver FFs, which are recognized as the most complicated parameters, given the relatively definite relationships of open-circuit voltage (V_{OC}) and J_{SC} with the energy level/photophysical properties of the donor/acceptor.[37–41] To intuitively display the evolution of FFs, the statistical FF distribution histograms are shown in Figures 3D–3F. Apparently, the FFs are greatly by influenced the relevant post-process. Notably, we highlight the exceptional FFs of TA-SVA-treated IDIC-C5Ph devices. An average FF of 79.22% is achieved, with the maximum of 80.03% among the best in OSCs. The high FF contributes to an impressive PCE of 14.56%, which ranks highest in simple IDIC family acceptors. The photoluminescence spectra indicate the efficient charge transfer between the donor and IDIC-C5Ph with and without treatments (Figure S12). However, the charge carrier mobilities, measured using the space charge-limited current (SCLC) model, show stronger and more balanced charge mobilities in TA-SVA optimized blends than under the as-cast and TA conditions (Table 1; Figure S13). Meanwhile, a higher exciton dissociation probability (P_{diss}) was detected in the TA-SVA-optimized devices (Figure S14). To deeply probe the charge carrier dynamics in IDIC-C5Ph-based OSCs, we conducted transient photocurrent (TPC) and transient photovoltage (TPV) measurements.[42] The charge extraction times (τ_{ext}) and recombination times (τ_{rec}) of photocarriers were determined by fitting the TPC decays under short-circuit conditions and the TPV decays under open-circuit conditions, respectively. As shown in Figure S15, the devices with as-cast, TA, and TA-SVA generate respective τ_{ext} values of 3.97, 3.45, and 2.64 μs. The τ_{ext} is shortened after TA-SVA, implying a faster charge extraction process. Simultaneously, the τ_{rec} (10.15 μs) after TA-SVA is more prolonged than the as-cast (3.24 μs) and TA (3.32 μs)-treated devices, suggesting a greatly suppressed recombination loss. These

Table 1. Device Parameters of OSCs under the Illumination of AM 1.5G, 100 mW cm^{-2}

Acceptor		V_{OC} (V)	J_{SC} (mA cm^{-2})	(J_{SC}^{EQE})[a]	FF (%)	FF_{max} (%)	PCE (%)[b]	μ_h/μ_e (10^{-4} cm^2 V^{-1} s^{-1})
IDIC-C4Ph	as-cast	0.952 (0.941 ± 0.010)	18.06 (17.75 ± 0.26)	17.31	76.77 (75.17 ± 1.55)	76.77	13.20 (13.00 ± 0.25)	2.36/2.45
	TA	0.942 (0.940 ± 0.007)	18.96 (18.73 ± 0.28)	18.25	78.05 (77.12 ± 0.95)	78.59	13.94 (13.77 ± 0.28)	5.46/5.93
	TA-SVA	0.976 (0.965 ± 0.011)	17.00 (16.81 ± 0.21)	16.52	62.31 (62.12 ± 1.82)	63.93	10.33 (10.12 ± 0.24)	3.20/2.47
IDIC-C5Ph	as-cast	0.961 (0.952 ± 0.011)	18.25 (17.98 ± 0.23)	17.30	71.37 (70.80 ± 0.63)	71.89	12.52 (12.24 ± 0.31)	1.90/1.59
	TA	0.964 (0.955 ± 0.008)	18.42 (18.09 ± 0.35)	17.57	72.19 (71.64 ± 0.64)	72.45	12.82 (12.60 ± 0.16)	2.25/1.94
	TA-SVA	0.948 (0.937 ± 0.011)	19.19 (18.89 ± 0.34)	18.65	80.02 (79.22 ± 0.81)	80.03	14.56 (14.34 ± 0.20)	5.42/6.26
IDIC-C6Ph	as-cast	0.949 (0.941 ± 0.011)	16.03 (15.67 ± 0.36)	15.69	66.68 (65.67 ± 0.93)	66.85	10.14 (9.87 ± 0.30)	2.84/1.06
	TA	0.936 (0.929 ± 0.007)	17.51 (17.09 ± 0.43)	16.91	70.26 (69.75 ± 0.42)	70.60	11.52 (11.22 ± 0.28)	2.94/1.87
	TA-SVA	0.946 (0.938 ± 0.008)	17.29 (17.04 ± 0.24)	16.77	76.83 (73.90 ± 2.75)	76.83	12.57 (11.72 ± 0.90)	3.52/2.34

[a]Integrated from the EQE spectrum.
[b]Average values with standard deviations based on at least 40 cells.

advantages are conducive to the record of such high FFs of over 80% in IDIC-C5Ph-based optimal devices.[43,44]

We then measured the external quantum efficiencies (EQEs) of three groups of solar cells under different treatments. All the calculated J_{SC}^{EQE} values from the EQE curves (Figures 3G–3I) show a small deviation with the recorded J_{SC} values (Table 1). Interestingly, we noted that all the TA-SVA-treated devices afford increased EQE responses of between 300 and 400 nm, probably indicating enhanced π−π* transitions along the conjugated backbones. Besides, all the EQE profiles reveal similar valleys around the wavelength of 400 nm, which is partly correlated with the decreased transmittance of ~400 nm of ITO substrates (Figure S16). Nevertheless, the three groups of OSCs still display very different EQE responses to post-treatments. As for IDIC-C4Ph devices (Figure 3G), a small red shift of 7 nm (onset wavelength) is detected after TA. However, the TA-SVA treatment produces a negative blue shift by 4 nm than the as-cast state. For IDIC-C5Ph cells, both the as-cast and TA treatments afford almost overlapped EQE curves, well consistent with their similar J_{SC} values. Distinctively, a remarkable red shift by 22 nm is generated after TA-SVA, accounting for the greatly increased J_{SC} values. While, for IDIC-C6Ph-based devices, both TA and TA-SVA give a close red shift of about 17 nm compared with the as-cast state. Even so, as for the three optimized devices (Figure S17), the EQE curve of IDIC-C6Ph remains narrower than IDIC-C4Ph and IDIC-C5Ph by about 16 nm, indicating insufficient optimization of molecular stacking in BHJ and is responsible for the disordered orientations of IDIC-C6Ph molecules. In contrast, the identical onset EQE spectra of IDIC-C5Ph and IDIC-C4Ph devices suggest that the weak crystallinity of IDIC-C5Ph is fully enhanced by TA-SVA in BHJ.

To better understand the variations in EQE, we measured the absorption spectra of PBDB-TF, the three acceptors, and their donor/acceptor blends (Figure S18). The absorption profiles of PBDB-TF are little disturbed by the post-processes (Figure S18A). However, the treatment to three acceptors causes obviously varied absorption properties. It seems that both TA and TA-SVA are inefficient for IDIC-C4Ph because of its inherent high crystallinity, while IDIC-C6Ph is highly sensitive to both process. For the IDIC-C5Ph film, only TA-SVA produces a greatly expanded and red-shifted absorption spectrum. Relative to acceptors, similar trends are found in blends. Notably, the PBDB-TF:IDIC-C5Ph blend affords almost identical trends with the neat acceptor. After TA-SVA, the spectrum of PBDB-TF:IDIC-C6Ph still produces a blue-shifted onset by 30 nm than PBDB-TF:IDIC-C4Ph and PBDB-TF:IDIC-C5Ph (Figure S19), leading to the narrower EQE response of the device, even with TA-SVA treatment, and is responsible for the unsatisfactory J_{SC} values of solar cells. Besides, despite the relatively weak absorption between 300 and 400 nm in blends, the EQE curves, especially for the TA-SVA-treated solar cells, exhibit relatively high EQE responses. This inconsistency between the blend absorptivity and EQE response is possibly correlated with the relatively strong photo-response of the organic π-conjugated materials in the shorter-wavelength range.

To probe deeply into the molecular stacking variations in acceptor films, we conducted GIWAXS studies on the films of IDIC-C*x*Ph (*x* = 4, 5, or 6) and the results are shown in Figure 4. We found that this subtle side-chain difference also endows the three acceptors with different responses to TA or TA-SVA. As Figure 4B shows, TA delivers better-defined π-π stacking spots for IDIC-C4Ph, denoting an enhanced face-on orientation. However, TA-SVA causes the film to form strong diffraction rings (Figure 4C) with the π-π $d_{spacing}$ increased from 3.43 to 3.53 Å. The random molecular orientations and loose π-π stacking are disadvantageous for the oriented charge transport of OSCs.[36] Minor improvements are found in TA-treated IDIC-C5Ph (Figure 4F) relative to the as-cast film. Intriguingly, dramatic changes are detected after TA-SVA treatment, with the film colors obviously changed from blue to chocolate and well consistent with their absorption film properties (Figure S18C). As shown in Figure 4G, TA-SVA endows the film with incomputable sharp and well-defined diffraction spots along the horizontal, vertical, and even the off-axis directions, suggesting the generation of many crystallites, and probably two π-π channels for charge transport in these crystallites, as observed in crystals (Figure 2).[45,46] This distinctive two-channel charge transport would facilitate the electron transfer in pure acceptor domains and suppress the charge combination in active layers, which is critical for the exceptional FFs achieved here. Demonstrated by the abundance of diffraction features and the emergence of crystallites, we show that TA-SVA effectively improved the crystallinity and molecular stacking in the IDIC-C5Ph film. In contrast, IDIC-C6Ph delivers enhanced diffraction rings, which ultimately dominates diffraction patterns under TA (Figure 4J). The raised serried diffraction rings indicate an increased crystallinity yet extremely random stacking orientations. TA-SVA slightly improves the face-on orientation. However, the diffraction rings still govern the patterns. To further study the charge transport behaviors of three acceptors under different treatments, we conducted SCLC measurements to determine their electron mobilities (μ_e) and the results are shown in Figures S20–S22. We found that, for the three as-cast films, IDIC-C4Ph shows the highest μ_e of 6.49 × 10^{-4} cm^2 V^{-1} s^{-1} because of its intrinsic good crystallinity and orientation. Notably, TA-SVA-optimized IDIC-C5Ph delivers the most competitive μ_e up to 10.51 × 10^{-4} cm^2 V^{-1} s^{-1} among these films. This could be because of its preferred crystallinity with 2D π-π channels for free carriers and again verifies the advantage of this special molecular assembly on charge transport.

To gain more information about the molecular stacking in BHJ, GIWAXS measurements were further performed on the as-cast BHJs and their TA- and TA-SVA-processed samples. The 2D images and π-π-stacking distances are collected in Figure S23 and Table S5, respectively. The corresponding line

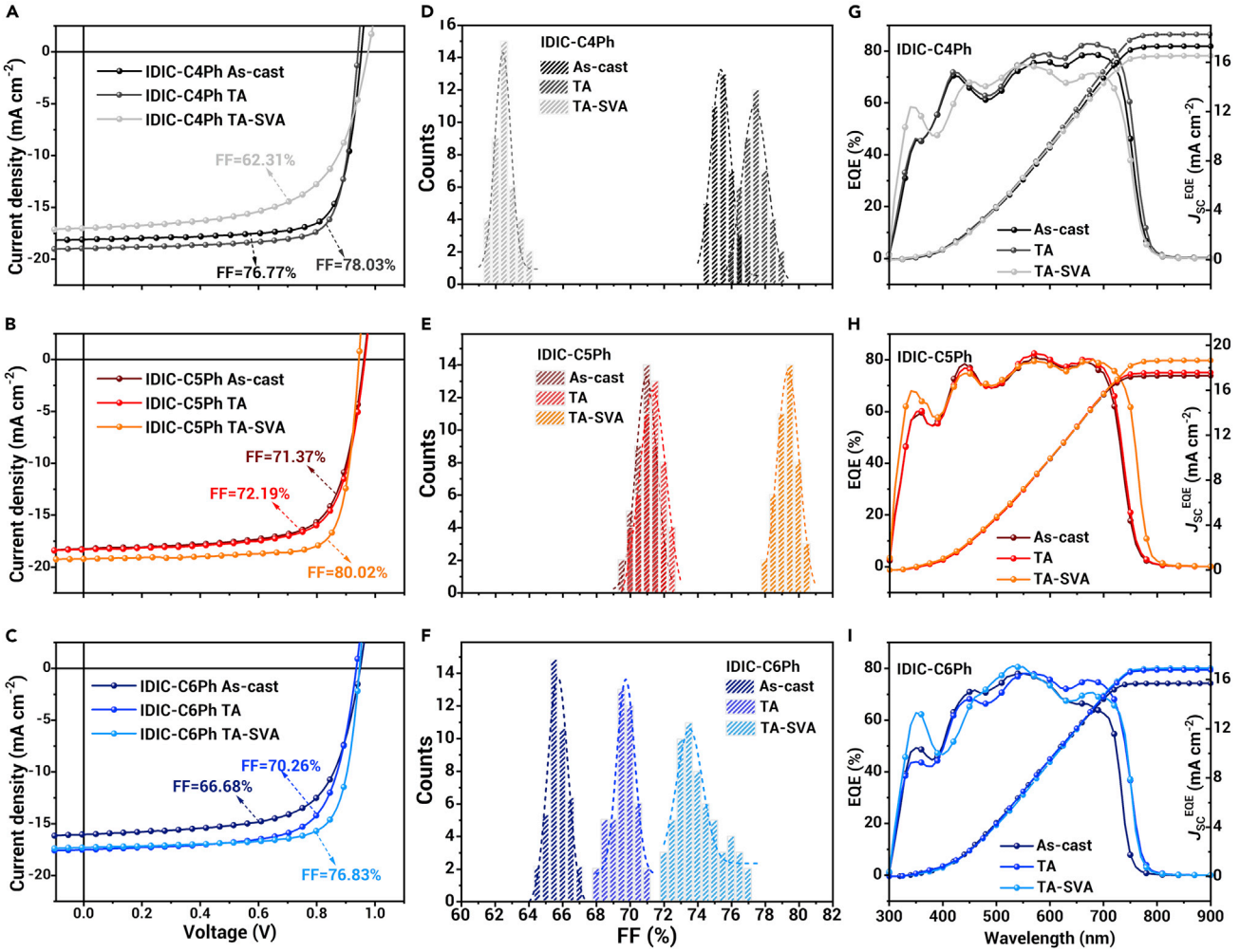

Figure 3. Photovoltaic Properties (A–C) The optimal *J-V* curves of three OSCs under as-cast, TA, and SVA treatments. (D–F) The statistical FF distribution histograms. (G–I) The EQE and integrated curves.

profiles are shown in Figures 5A, 5E, and 5I. A moderate diffraction peak at Q_z = 1.78 Å^{-1} is detected from the PBDB-TF:IDIC-C4Ph as-cast film, corresponding to the face-on orientation with a $d_{\pi\text{-}\pi}$ of 3.53 Å and a π-π crystal coherence length (CCL) of 18.21 Å. After TA treatment, the π-π diffraction plot enhances and migrates to a larger Q_z = 1.83 Å^{-1}, indicating a stronger and more compact π-π stacking with $d_{\pi\text{-}\pi}$ of 3.44 Å and increased CCL of 26.22 Å. This denotes that the molecular stacking in TA-optimized BHJ grows more orderly in the vertical orientation. However, TA-SVA destroys the preferred orientation with an emerging series of diffraction rings (Figure S23C), indicating disordered molecular orientations. Although TA-SVA to the IDIC-C4Ph-based blend affords a raised π-π diffraction with a similar $d_{\pi\text{-}\pi}$ of 3.53 Å relative to the as-cast blend, the negative orientations are adverse to the oriented charge transport of OSCs. For the PBDB-TF:IDIC-C5Ph blend, as shown in Figure 5E, TA gives rise to a minor improvement of molecular stacking, with a slightly enhanced π-π diffraction at Q_z = 1.76 Å^{-1} and a similar CCL of ~19 Å. Impressively, TA-SVA generates a distinct increase of π-π diffraction, accompanied by a remarkably narrowed $d_{\pi\text{-}\pi}$ from 3.58 to 3.34 Å, an increased CCL of 30.10 Å, and long-range orderly packing plots. This multilevel better-organized molecular stacking could be contributed to by the efficient molecular assembly of IDIC-C5Ph under TA-SVA and is considered to be a critical contributor to the superior charge transport (Table 1) and FFs of over 80%. For the IDIC-C6Ph-based blend, the polymeric donor apparently suppresses the overly disordered orientations of IDIC-C6Ph and promotes the face-on orientations in the TA blend (Figure 5I), with a narrowed $d_{\pi\text{-}\pi}$ from 3.58 to 3.48 Å and an increased CCL from 16.11 to 22.44 Å. Compared with TA treatment, TA-SVA slightly improves the face-on orientation with the same $d_{\pi\text{-}\pi}$ and a slightly larger CCL of 25.13 Å. However, similar with the diffraction pattern of the IDIC-C6Ph film (Figure 4K), considerable disordered molecular orientation still exists in the BHJ, partly accounting for the unfavorable J_{SC} values of OSCs.

Besides the molecular orientations, the BHJ morphologies play another key role in determining the charge transport and efficiencies. Thus, we conducted transmission electron microscopy and atomic force microscopy (AFM) studies to probe the morphologies and the results are shown in Figures 5 and S24–S26, respectively. Well-distributed nanofiber interpenetrating networks were found from both the as-cast and TA-treated PBDB-TF:IDIC-C4Ph films (Figures 5B and 5C), indicating the preferred phase separation behaviors. Meanwhile, the corresponding AFM images show smooth fibrous surfaces with low root-mean-square (RMS) roughness of ~2.0 nm (Figure S24). Combined with their good molecular orientations (Figure 4A), such a morphology feature is beneficial for the efficient charge transport and satisfactory PCEs and FFs. However, after TA-SVA treatment, nanofibers disappeared and there was serious phase separation with chunky large aggregates assembled. Similar aggregates are also found from the AFM patterns, leading to a bumpy surface with a more than doubled RMS of 4.48 nm (Figure S24), which is the cause of the dramatic drops of FFs and PCEs in devices (Table 1).

With the side chain increased from C4Ph to C5Ph, the IDIC-C5Ph-based BHJ generates fairly different behaviors. TA treatment affords a similar morphology, with the as-cast sample lacking nanofiber-shaped phase

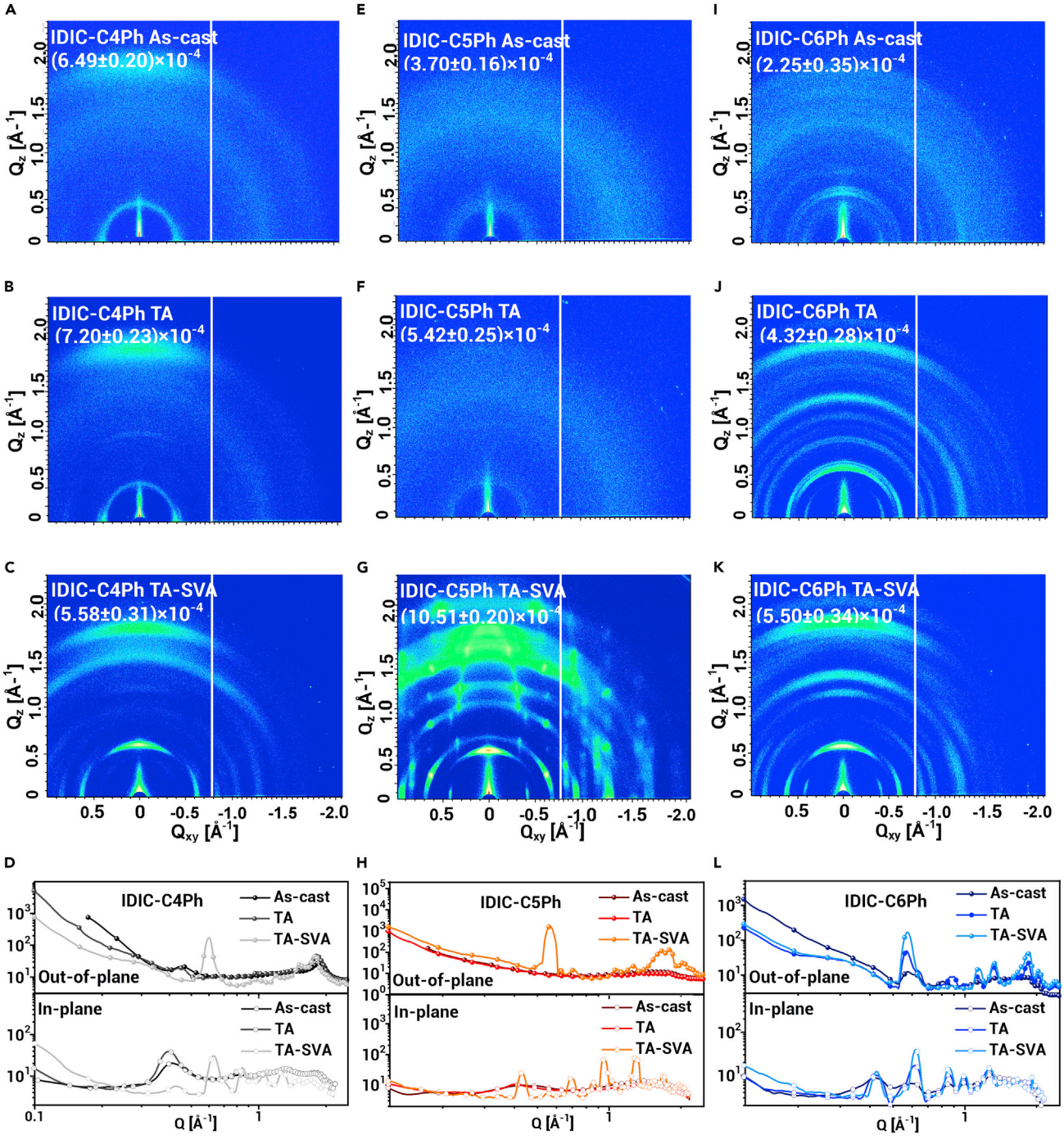

Figure 4. GIWAXS Studies GIWAXS scattering patterns of (A–C) IDIC-C4Ph, (E–G) IDIC-C5Ph, and (I–K) IDIC-C6Ph films under different treatments (the numbers represent the electron mobilities based on an SCLC model). (D, H, and L) The corresponding line profiles.

separation (Figures 5G and S25). These observations are well consistent with the ineffective optimization of IDIC-C5Ph crystallinity (Figure 4F), the absorption variations of IDIC-C5Ph and blend films (Figure S18), and the moderate PCEs and FFs of cells. Significantly different from the deteriorative IDIC-C4Ph-based BHJ, TA-SVA promotes the appropriate phase separation of PBDB-TF:IDIC-C5Ph with dense thread-like nanoscale fibrous aggregates. Also, nanoscale crystallites can be observed from the corresponding AFM image (Figure S25C), which probably possess comparable diamond crossing molecular assembly. The compact molecular stacking of crystalline IDIC-C5Ph after TA-SVA is beneficial for the formation of pure acceptor crystalline domains in the BHJ, and enhances the charge transport as well as phase separation behavior. The characteristic BHJ texture and compact face-on orientation (Figure 5E) are desirable for the efficient charge generation and the dissociation process, accounting for the boosted efficiencies and highly competitive FFs. However, the PBDB-TF:IDIC-C6Ph blend affords thick fibrous aggregates of over 200 nm (Figures 5J and 5K) and rough surfaces (Figure S26). This inferior as-cast morphology could increase the recombination loss inside the BHJ, as indicated by the shortest τ_{rec} values among three as-cast devices (Figure S27), leading to low FF and J_{SC} values of OSCs. TA negligibly alters BHJ morphology. In contrast, TA-SVA affords smaller-scale nanofibers in the BHJ. However, detectable low-lying trenches and thereby a greater RMS of 4.45 nm occurs during TA-SVA (Figure S26C). Furthermore,

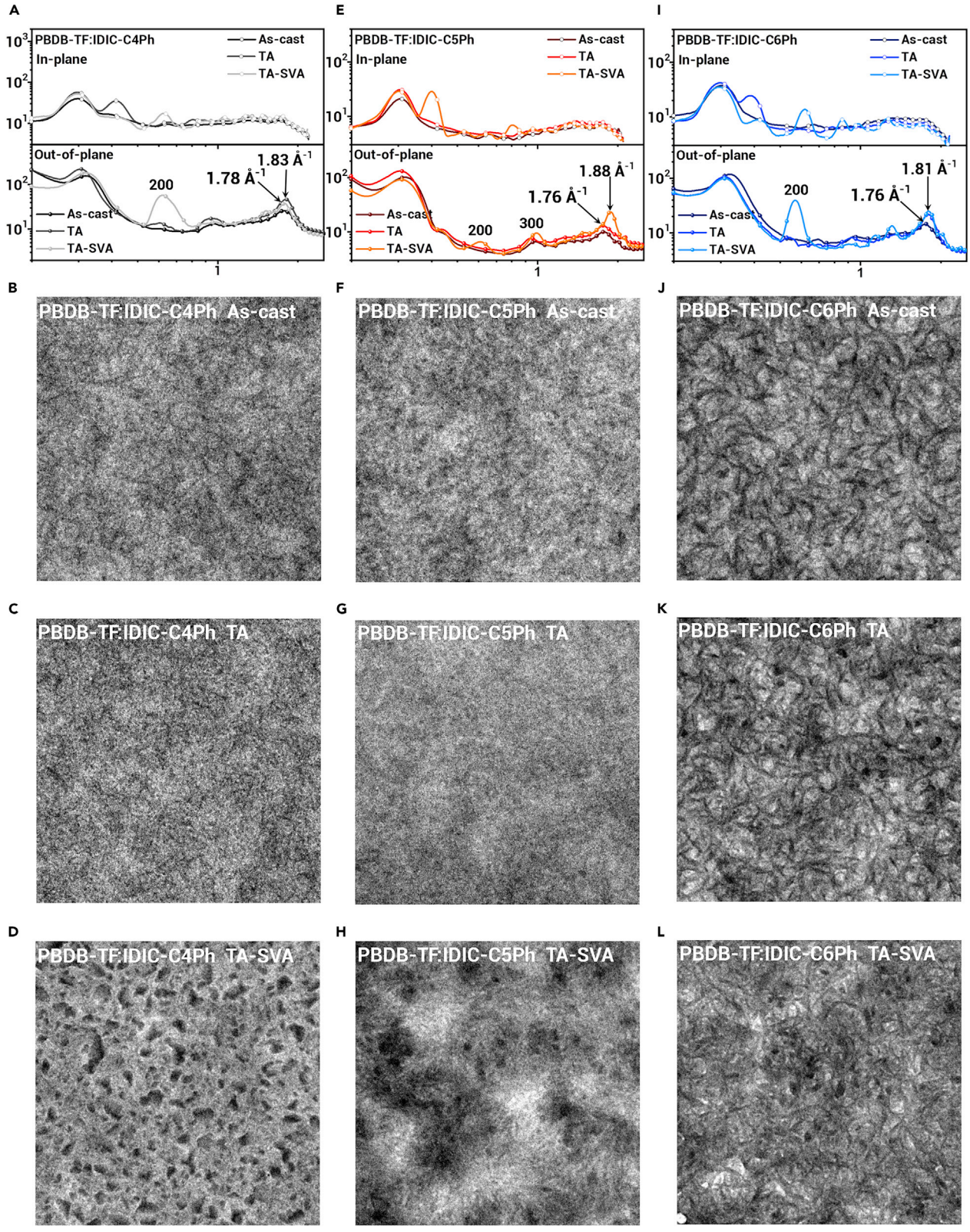

Figure 5. BHJ Morphologies (A, E, and I) The line profiles (solid line, OOP direction; point plot, IP direction) of GIWAXS studies of three blends. The transmission electron microscopy images (1.25 × 1.25 μm) of BHJ films of (B–D) PBDB-TF:IDIC-C4Ph, (F–H) PBDB-TF:IDIC-C5Ph, and (J–L) PBDB-TF:IDIC-C6Ph under different treatments.

the grooved hard-to-tailor morphology of this TA-SVA-treated BHJ is probably the reason for the undesired repeatability of the solar cells.

Also, it is well accepted that developing thickness-insensitive material systems is one critical foundation for large-scale practical production, where the final PCEs could be seriously harmed by the thickness inhomogeneity of large-scale active layers. Nowadays, in most cases, high PCEs could be recorded under an optimal active layer thicknesses of ~100 nm. However, the efficiencies usually decrease very fast with increase of film thickness,

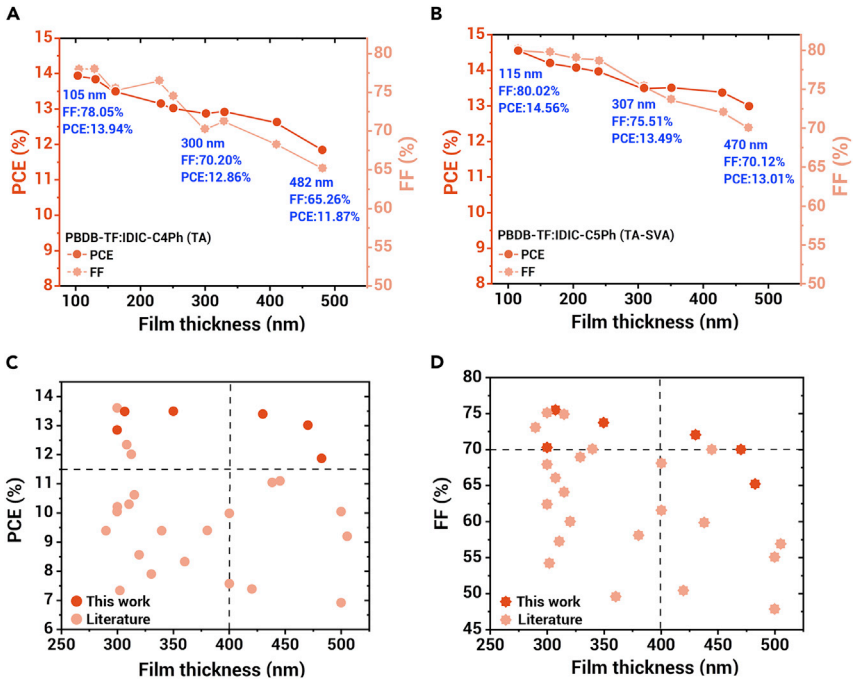

Figure 6. Thick-Film OSCs The PCEs and FFs of the optimal solar cells (A) PBDB-TF:IDIC-C4Ph and (B) PBDB-TF:IDIC-C5Ph versus the active layer film thickness. Comparison of the thick-film OSCs with representative (C) PCEs and (D) FFs values reported in the literature and in this work.

which is mainly ascribed to the dramatic loss of FFs. Therefore, given the very high FFs of over 80% and the efficient TCCT behaviors in optimized PBDB-TF:IDIC-C5Ph solar cells, there could be ample room for the preservation of good FFs and the suppression of serious charge recombination in thick BHJs. Thus, we further fabricated a series of devices with varied active layer film thickness from 100 to ~500 nm to probe the thickness-dependence behaviors. For a clear comparison, the common single-channel charge transport acceptor IDIC-C4Ph-based devices were also studied. The photovoltaic parameters of the optimal PBDB-TF:IDIC-C4Ph and PBDB-TF:IDIC-C5Ph cells under different film thicknesses are shown in Figures 6A, 6B, and S28, and Table S6. Generally, with the increase of film thickness, the V_{OC} values slightly decrease, but the J_{SC} parameters mildly increase due to the compromise of raised photon-harvesting and charge combination in thick films. Nevertheless, the dramatic roll-off of FF is the main cause of the drop of PCE. Specifically, the IDIC-C4Ph-based devices deliver the optimal PCE of 13.94% with a high FF of 78.05% under a thin film of 105 nm. With the film thickness increased to 300 nm, the corresponding FF reduced to 70.20% with a PCE of 12.86%. When the thickness reached 482 nm, an FF of 65.26% (83.61% of the initial value) with a PCE of 11.87% was recorded. Despite this moderate performance, the PCEs and FFs under such a high film thickness of ~500 nm are superior to most values reported (Table S7).

With regard to IDIC-C5Ph-based OSCs, the optimal PCE of 14.56% with a corresponding FF up to 80.02% was measured under a 115-nm active layer. With a film thickness of 307 nm, an impressive FF of 75.51% (94.36% of initial value) is preserved, which is the highest FF for OSCs of more than 300-nm film thickness to date and is even comparable with most of the reported efficient OSCs with active layers of ~100 nm. This slight roll-off of FF under 307 nm contributes to the high PCE of 13.49% with 92.65% of optimal PCE preserved. It is known that the efficient acceptor Y6 can produce a very high PCE of 15.7% in a single BHJ of 150 nm with a good FF of 74.8%.[5] However, in 300 nm thick-film devices, the FF dropped to 62.3% (83.29% of initial value). As a result, despite the raised J_{SC} value of Y6-based 300 nm thick-film devices, the huge decrease of FF led to a seriously reduced PCE of 13.6%. More excitingly for IDIC-C5Ph-based OSCs with a high thickness of 470 nm, a PCE of 13.01% with an FF of 70.12% was measured, with 89.35% of the initial PCE retained (relative to the 115 nm device). Hereon, we want to highlight the 13.01% PCE with over 70% FF under such a high active layer thickness close to 500 nm, which ranks best among reports in thick-film OSCs to date. Figures 6C and 6D depict the location of PCEs and related FFs under film thicknesses of no less than 300 nm. We observe that most of the reported efficient thick-film OSCs with PCEs over 10% fall between 300 and 350 nm. With the increase of film thickness, the FFs dramatically decreased leading to inferior efficiencies. Figure 6 clearly highlights the highly efficient thick-film OSCs based on IDIC-C4Ph and IDIC-C5Ph reported in this work. Notably, these results indicate the outstanding thickness-insensitive properties of IDIC-C5Ph-based devices, and suggest the great promise of efficient TCCT properties in fabricating high-performance thick-film OSCs.

Conclusion

In summary, we clearly show the great impact of side chains on materials and photovoltaic performance. Through a simple and subtle modification of side chains, three acceptors IDIC-CxPh (x = 4, 5, or 6) differ greatly in crystallinity, molecular stacking, BHJ morphology, photovoltaic properties, and their best post-process conditions. The shorter C4Ph chain endows IDIC-C4Ph with higher crystallinity and ordered molecular stacking, generating the optimum BHJ morphology and PCE (13.94%) under mild TA. The longer C6Ph chain leads to an extremely disordered orientations of molecules, affording an only 12.57% efficiency after optimizations. Unexpectedly, the modest C5Ph chain induces the lowest film crystallinity among the three acceptors, but the densest diamond crossing two-channel π-π stacking in crystals, which affords promising TCCT properties. With TA-SVA, the molecular assembly of the IDIC-C5Ph film is greatly enhanced, affording a remarkably improved phase separation, compact face-on orientation, and PCEs up to 14.56% with excellent FFs up to 80.02%. Furthermore, the extraordinary TCCT properties of IDIC-C5Ph endows the solar cells with outstanding thickness-insensitive behaviors, generating a high PCE of 13.01% with very impressive FFs reaching 70% in 470 nm thick-film OSCs. These findings directly indicate that the subtle adjustment of non-conjugated side chains could have a huge impact on the molecular assembly and photovoltaic performance, and the suitable side-chain-induced TCCT property is of great promise in fabricating high-efficiency thick-film OSCs.

REFERENCES

1. Yu, G., Gao, J., Hummelen, J.C., et al. (1995). Polymer photovoltaic cells—enhanced efficiencies via a network of internal donor-acceptor heterojunctions. Science ***270***, 1789–1791.
2. Li, G., Zhu, R., and Yang, Y. (2012). Polymer solar cells. Nat. Photon. ***6***, 153–161.

3. Halls, J.J.M., Pichler, K., Friend, R.H., et al. (1996). Exciton diffusion and dissociation in a poly(p-phenylenevinylene)/C-60 heterojunction photovoltaic cell. Appl. Phys. Lett. ***68***, 3120–3122.
4. Lin, Y., Wang, J., Zhang, Z., et al. (2015). An electron acceptor challenging fullerenes for efficient polymer solar cells. Adv. Mater. ***27***, 1170–1174.
5. Yuan, J., Zhang, Y., Zhou, L., et al. (2019). Single-junction organic solar cell with over 15% efficiency using fused-ring acceptor with electron-deficient core. Joule ***3***, 1140–1151.
6. Liu, Q., Jiang, Y., Jin, K., et al. (2020). 18% Efficiency organic solar cells. Sci. Bull. ***65***, 272–275.
7. Cui, Y., Yao, H., Zhang, J., et al. (2020). Single-junction organic photovoltaic cells with approaching 18% efficiency. Adv. Mater. ***32***, 1908205.
8. An, Q., Wang, J., Ma, X., et al. (2020). Two compatible polymer donors contribute synergistically for ternary organic solar cells with 17.53% efficiency. Energy Environ. Sci. ***13***, 5039–5047.
9. Han, J., Bao, F., Huang, D., et al. (2020). A universal method to enhance flexibility and stability of organic solar cells by constructing insulating matrices in active layers. Adv. Funct. Mater. ***30***, 2003654.
10. Li, D., Zhu, L., Liu, X., et al. (2020). Enhanced and balanced charge transport boosting ternary solar cells over 17% efficiency. Adv. Mater. ***32***, 2002344.
11. Yao, J., Qiu, B., Zhang, Z., et al. (2020). Cathode engineering with perylene-diimide interlayer enabling over 17% efficiency single-junction organic solar cells. Nat. Commun. ***11***, 2726.
12. Luo, Z., Ma, R., Liu, T., et al. (2020). Fine-tuning energy levels via asymmetric end groups enables polymer solar cells with efficiencies over 17%. Joule ***4***, 1236–1247.
13. Zhu, C., Yuan, J., Cai, F., et al. (2020). Tuning the electron-deficient core of a non-fullerene acceptor to achieve over 17% efficiency in a single-junction organic solar cell. Energy Environ. Sci. ***13***, 2459–2466.
14. McDowell, C., Abdelsamie, M., Toney, M.F., and Bazan, G.C. (2018). Solvent additives: key morphology-directing agents for solution-processed organic solar cells. Adv. Mater. ***30***, 1707114.
15. Bin, H., Yang, Y., Peng, Z., et al. (2018). Effect of alkylsilyl side-chain structure on photovoltaic properties of conjugated polymer donors. Adv. Energy Mater. ***8***, 1702324.
16. Zhang, G., Xu, X., Bi, Z., et al. (2018). Fluorinated and alkylthiolated polymeric donors enable both efficient fullerene and nonfullerene polymer solar cells. Adv. Funct. Mater. ***28***, 1706404.
17. Zhou, H., Yang, L., Stuart, A.C., et al. (2011). Development of fluorinated benzothiadiazole as a structural unit for a polymer solar cell of 7% efficiency. Angew. Chem. Int. Ed. ***50***, 2995–2998.
18. Wang, X., Dou, K., Shahid, B., et al. (2019). Terpolymer strategy toward high-efficiency polymer solar cells: integrating symmetric benzodithiophene and asymmetrical thieno [2,3-f]benzofuran segments. Chem. Mater. ***31***, 6163–6173.
19. Fu, H., Wang, Z., and Sun, Y. (2019). Polymer donors for high-performance non-fullerene organic solar cells. Angew. Chem. Int. Ed. ***58***, 4442–4453.
20. Gao, W., Zhang, M., Liu, T., et al. (2018). Asymmetrical ladder-type donor-induced polar small molecule acceptor to promote fill factors approaching 77% for high-performance nonfullerene polymer solar cells. Adv. Mater. ***30***, 1760–1768.
21. Liu, Y., Li, M., Zhou, X., et al. (2018). Nonfullerene acceptors with enhanced solubility and ordered packing for high-efficiency polymer solar cells. ACS Energy Lett. ***3***, 1832–1839.
22. Aldrich, T.J., Swick, S.M., Melkonyan, F.S., and Marks, T.J. (2017). Enhancing indacenodithiophene acceptor crystallinity via substituent manipulation increases organic solar cell efficiency. Chem. Mater. ***29***, 10294–10298.
23. Jiang, H., Han, C., Li, Y., et al. (2020). Rational mutual interactions in ternary systems enable high-performance organic solar cells. Adv. Funct. Mater. ***30***, 2007088.
24. Liu, Z., Zhang, G., and Zhang, D. (2018). Modification of side chains of conjugated molecules and polymers for charge mobility enhancement and sensing functionality. Acc. Chem. Res. ***51***, 1422–1432.
25. Li, X., Huang, H., Angunawela, I., et al. (2020). Effects of short-axis alkoxy substituents on molecular self-assembly and photovoltaic performance of indacenodithiophene-based acceptors. Adv. Funct. Mater. ***30***, 1906855.
26. Fei, Z., Eisner, F.D., Jiao, X., et al. (2018). An alkylated indacenodithieno[3,2-b]thiophene-based nonfullerene acceptor with high crystallinity exhibiting single junction solar cell efficiencies greater than 13% with low voltage losses. Adv. Mater. ***30***, 1705209.
27. Luo, Z., Sun, C., Chen, S., et al. (2018). Side-chain impact on molecular orientation of organic semiconductor acceptors: high performance nonfullerene polymer solar cells with thick active layer over 400 nm. Adv. Energy Mater. ***8***, 1800856.
28. Li, S., Li, C., Shi, M., and Chen, H. (2020). New phase for organic solar cell research: emergence of y-series electron acceptors and their perspectives. ACS Energy Lett. ***5***, 1554–1567.
29. Jiang, K., Wei, Q., Lai, J.Y.L., et al. (2019). Alkyl chain tuning of small molecule acceptors for efficient organic solar cells. Joule ***3***, 3020–3033.
30. Zhu, L., Zhang, M., Zhou, G., et al. (2020). Efficient organic solar cell with 16.88% efficiency enabled by refined acceptor crystallization and morphology with improved charge transfer and transport properties. Adv. Energy Mater. ***10***, 1904234.
31. Li, Y., Zheng, N., Yu, L., et al. (2019). A simple phenyl group introduced at the tail of alkyl side chains of small molecular acceptors: new strategy to balance the crystallinity of acceptors and miscibility of bulk heterojunction enabling highly efficient organic solar cells. Adv. Mater. ***31***, 1807832.
32. Fan, Q., Wang, Y., Zhang, M., et al. (2018). High-performance as-cast nonfullerene polymer solar cells with thicker active layer and large area exceeding 11% power conversion efficiency. Adv. Mater. ***30***, 1704546.
33. Yiu, A.T., Beaujuge, P.M., Lee, O.P., et al. (2012). Side-chain tunability of furan-containing low-band-gap polymers provides control of structural order in efficient solar cells. J. Am. Chem. Soc. ***134***, 2180–2185.
34. Jiang, H., Li, X., Wang, J., et al. (2019). Ternary polymer solar cells with high efficiency of 14.24% by integrating two well-complementary nonfullerene acceptors. Adv. Funct. Mater. ***29***, 1903596.
35. Cheng, P., Wang, P., Xu, Z., et al. (2019). Ligand-size related dimensionality control in metal halide perovskites. ACS Energy Lett. ***4***, 1830–1838.
36. Crystallographic data of IDIC-C4Ph, IDIC-C5Ph and IDIC-C6Ph were deposited in the Cambridge Crystallographic Data Center with CCDC number of 1947277, 1947278 and 1947279, respectively.
37. Dey, S. (2019). Recent progress in molecular design of fused ring electron acceptors for organic solar cells. Small ***15***, 1900134.
38. Eastham, N.D., Dudnik, A.S., Harutyunyan, B., et al. (2017). Enhanced light absorption in fluorinated ternary small-molecule photovoltaics. ACS Energy Lett. ***2***, 1690–1697.
39. Zaborova, E., Chavez, P., Bechara, R., et al. (2013). Thiazole as a weak electron-donor unit to lower the frontier orbital energy levels of donor-acceptor alternating conjugated materials. Chem. Commun. (Camb.) ***49***, 9938–9940.
40. Lopez, S.A., Sanchez-Lengeling, B., de Goes Soares, J., and Aspuru-Guzik, A. (2017). Design principles and top non-fullerene acceptor candidates for organic photovoltaics. Joule ***1***, 857–870.
41. Wu, Q., Deng, D., Zhang, J., et al. (2019). Fluorination-substitution effect on all-small-molecule organic solar cells. Sci. China Chem. ***62***, 837–844.
42. MacKenzie, R.C.I., Shuttle, C.G., Chabinyc, M.L., and Nelson, J. (2012). Extracting microscopic device parameters from transient photocurrent measurements of P3HT:PCBM solar cells. Adv. Energy Mater. ***2***, 662–669.
43. Li, Y., Liu, D., Wang, J., et al. (2017). Crystalline medium-bandgap light-harvesting donor material based on β-naphthalene asymmetric-modified benzodithiophene moiety toward efficient polymer solar cells. Chem. Mater. ***29***, 8249–8257.
44. Jiang, H., Li, X., Wang, H., et al. (2020). Significantly enhanced molecular stacking in ternary bulk heterojunctions enabled by an appropriate side group on donor polymer. Adv. Sci. ***7***, 1903455.
45. Hu, J., Oswald, I.W.H., Hu, H., et al. (2019). Aryl-perfluoroaryl interaction in two-dimensional organic-inorganic hybrid perovskites boosts stability and photovoltaic efficiency. ACS Mater. Lett. ***1***, 171–176.
46. He, Q., Shahid, M., Wu, J., et al. (2019). Fused cyclopentadithienothiophene acceptor enables ultrahigh short-circuit current and high efficiency >11% in as-cast organic solar cells. Adv. Funct. Mater. ***29***, 1904956.

ACKNOWLEDGMENTS

The authors are deeply grateful to the National Natural Science Foundation of China (21502205, 51773220, 51703104, and 51873227) and DICP&QIBEBT (UN201805) for financial support. X.C.B. deeply thanks the Youth Innovation Promotion Association CAS (2016194). R.Q.Y. gives thanks to the "Chutian Scholar Program" of Hubei province. The work is also supported by the Dalian National Laboratory for Clean Energy for Clean Energy (DNL), CAS. The authors thanks Prof. Chunming Yang from the Shanghai Synchrotron Radiation Facility for useful discussions.

AUTHOR CONTRIBUTIONS

Y.H.L. designed the research and wrote the paper. L.Y., C.Y.H., and J.X.W. performed materials synthesis. L.L.C. and Z.T.L. characterized the single crystals. H.X.J. assisted with the photovoltaic measurements. N.Z. performed the GIWAXS measurements. M.L.S., R.Q.Y., and X.C.B. supervised the study. X.C.B. revised the paper.

DECLARATION OF INTERESTS

The authors declare no competing interests.

SUPPLEMENTAL INFORMATION

Supplemental Information can be found online at https://doi.org/10.1016/j.xinn.2021.100090.

LEAD CONTACT WEBSITE

https://www.researchgate.net/profile/Xichang_Bao.

The Innovation, Volume *2*

Supplemental Information

Subtle Side Chain Triggers Unexpected Two-Channel Charge Transport Property Enabling 80% Fill Factors and Efficient Thick-Film Organic Photovoltaics

Yonghai Li, Lu Yu, Liangliang Chen, Chenyu Han, Huanxiang Jiang, Zitong Liu, Nan Zheng, Jiuxing Wang, Mingliang Sun, Renqiang Yang, and Xichang Bao

Supporting Information

Subtle Side Chain Triggers Unexpected Two-Channel Charge Transport Property Enabling 80% Fill Factors and Efficient Thick-Film Organic Photovoltaics

Yonghai Li,*[a,c] Lu Yu,[a,b] Liangliang Chen,[d] Chenyu Han,[a] Huanxiang Jiang,[a] Zitong Liu,[d] Nan Zheng,*[e] Jiuxing Wang,[f] Mingliang Sun,[b] Renqiang Yang*[a,g] and Xichang Bao*[a,c]

[a] CAS Key Laboratory of Bio-based Materials, Qingdao Institute of Bioenergy and Bioprocess Technology, Chinese Academy of Sciences, Qingdao 266101, China.

[b] School of Material Science and Engineering, Ocean University of China, Qingdao 266100, China

[c] Functional Laboratory of Solar Energy, Shandong Energy Institute, Qingdao 266101, China

[d] Beijing National Laboratory for Molecular Sciences, CAS Key Laboratory of Organic Solids, Institute of Chemistry, Chinese Academy of Sciences, Beijing 100190, China

[e] State Key Laboratory of Luminescent Materials and Devices, South China University of Technology, Guangzhou 510640, China.

[f] School of Materials Science and Engineering, Qingdao University, Qingdao 266071, China

[g] Key Laboratory of Optoelectronic Chemical Materials and Devices (Ministry of Education), School of Chemical and Environmental Engineering, Jianghan University, Wuhan 430056, China

E-mail: liyh@qibebt.ac.cn (Y. L.); zhengn@scut.edu.cn (N. Z.); yangrq@qibebt.ac.cn (R. Y.); baoxc@ qibebt.ac.cn (X. B.)

Experimental Procedures

Materials and Characterization Techniques

Donor material PBDB-TF were purchased from Solarmer Materials Inc. The compound IDT was purchased from Derthon Co. All solvents and reagents were purchased from Alfa Aesar, Sigma-Aldrich, et al., which were utilized directly unless stated otherwise.

^{1}H NMR and ^{13}C NMR spectra were recorded on Bruker AVANCE III 600 MHz or Bruker AVANCE III 400 MHz spectrometer at 298 K. TGA measurement was performed using a SDT Q600 V20.9 Build 20 at a heating rate of 10 ^{o}C min^{-1} under a nitrogen atmosphere. The absorption spectra were recorded using a Hitachi U-4100 UV-Vis scanning spectrophotometer. Cyclic voltammetry (CV) measurements were performed on a CHI660D electrochemical workstation, equipped with a three-electrode cell consisting of a platinum working electrode, a saturated calomel electrode (SCE) as reference electrode and a platinum wire counter electrode. CV measurements were carried out in anhydrous acetonitrile containing 0.1 M *n*-Bu_4NPF_6 as a supporting electrolyte under an argon atmosphere at a scan rate of 100 mV s^{-1} assuming that the absolute energy level of Fc/Fc^{+} was -4.80 eV. Thin films were deposited from $CHCl_3$ solution onto the working electrodes. Grazing incidence wide-angle X-ray scattering (GIWAXS) patterns were acquired by detector Pilatus3R 1M, Dectris (X-ray Source: MetalJet-D2, Excillum). Transmission electron microscopy (TEM) images were obtained by using a HITACHI H-7650 electron microscope with an acceleration voltage of 100kV. Atomic force microscopy (AFM) images were obtained using Agilent 5400 scanning probe microscope in tapping mode with MikroMasch NSC-15 AFM tips. The X-ray crystallographic data were collected from Single crystal X-ray diffractometer (Synergy-R, Hybrid-CMOS 2D detector).

Device Fabrication and Evaluations

Photovoltaic devices were fabricated with a conventional device structure of ITO/PEDOT:PSS/PBDB-TF:IDIC-C*x*Ph/PDINO/Al. The patterned ITO glass (sheet resistance = 15 Ω/ square) was pre-cleaned in an ultrasonic bath of acetone and isopropyl alcohol and treated in an ultraviolet-ozone chamber (PREEN II-862) for 6 min. Then a thin layer (about 30 nm) of PEDOT:PSS was spin-coated onto the ITO glass at 4000 rpm and baked at 150 ^{o}C for 15 min. Solutions of PBDB-TF/ IDIC-C*x*Ph in chlorobenzene (18 mg/mL, total concentration) were stirred overnight and warmed to 50 ^{o}C for 30 mins before spin-coating on the PEDOT:PSS layer to form the active layer about 100±30 nm. The thickness of the active layer was measured using a Veeco Dektak 150 profilometer. Then PDINO solution (in CH_3OH, 1mg/mL) was spin-coating at 3000 rpm to form the electron transfer layer. Finally, Al (60 nm) metal electrode was thermal evaporated under about 4×10^{-4} Pa and the device area was 0.1 cm^2 defined by shadow mask.

The current density–voltage (*J–V*) characteristics were recorded with a Keithley 2400 source measurement under simulated 100 mW cm^{-2} irradiation from a SciSun-300 solar simulator. The *J–V* measurements were conducted without a correction window. The external quantum efficiencies (EQEs) were analysed EQE measurments through the Enlitech QE-R3011 quantum efficiency measurement system. The light intensity was calibrated with a standard single-crystal Si photovoltaic cell. The beam size is 5 cm × 5 cm. The voltage step and delay time were 10 mV and 3 ms, respectively. The scan started from −0.2 V to 1.4 V. The hole mobility and electron mobility were measured by space-charge-limited current (SCLC) method with a device

configuration of ITO/PEDOT:PSS/active layer/MoO_3/Al and ITO/ZnO/active layer/PFN/Al structure, respectively. The SCLC is described by the Mott–Gurney law:

$J = 9\varepsilon\mu V^2/(8L^3)$

where ε represents the dielectric constant of the metal, and μ is the carrier mobility, V is the voltage drop across the device and L is the thickness of the active layer.

The details for single crystals cultivation

The acceptor (IDIC-C4Ph, IDIC-C5Ph and IDIC-C6Ph) was dissolved in chloroform (~1mg/mL, 8 mg) and sealed in a small vial (volume: 15 mL) by aluminium-foil paper. Then several (4~6) pinholes were made on the foil paper by fine needle and put the small vial into a large-sized vial (volume: 50 mL), which contains 10 mL n-hexane. Finally, the large-sized vial was tightly sealed and put into a quiet and dark place at room temperature for 5~7 days to culture the single crystals.

The details for TA-SVA post-treatment

After spin-coating the active layer, or the neat donor or acceptor film onto ITO/glass substrates, the sample was put into a Petri dish (dia. 20 cm). Then 75 μL chlorobenzene (CB) was injected evenly from the sides. Given the high boiling point (132.2 °C) of CB and the low vapour pressure at room temperature, the Petri dish containing the samples was put onto a heating stage (80 °C) in glove box to accelerate the volatilization of chlorobenzene, and kept for 10 min to fully realize the solvent vapour annealing. During the SVA, we can observe the emergence of CB vapour which was coagulated in the cover of the Petri dish from about 2.5 min to about 8 min. Thus the SVA treatment in this study is aided by TA treatment (TA-SVA post-treatment).

The thermal annealing (TA) treatment

TA treatments were performed on a heating stage (80 °C) and kept for 10 min in the glove box.

The synthetic details of acceptors

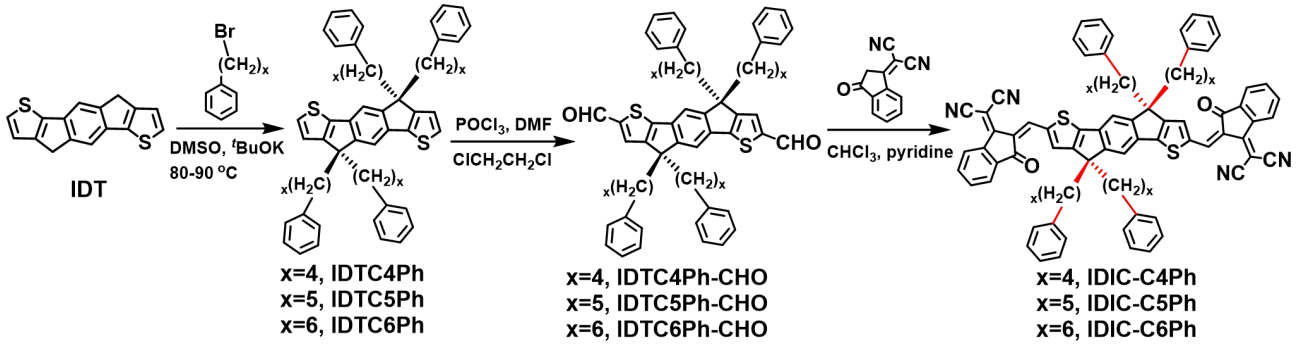

Scheme S1. The synthetic routes of IDIC-CxPh (x=4, 5, 6).

The IDIC-C4Ph was synthesized according to our previous report (*Adv. Mater*. 2019, 1807832).

Synthesis of IDTC5Ph: IDT (532.8 mg, 2.0 mmol) was dispersed in 15 mL dry DMSO and stirred under argon atmosphere. Then ^{t}BuOK (1.35 g, 12.0 mmol) was added in small portions. After then, the solution was heated at 80 ^{o}C for 1.0 hr. Subsequently, (5-bromopentyl)benzene (2.27 g, 1.85 mL, 10.0 mmol) was dropwise added into the solution and heated at 85-90 ^{o}C for another 5.0 hrs. When the solution cooled into room temperature, it was poured into ice water and extracted with dichloromethane (50 mL×3), dried with anhydrous Na_2SO_4, and removed the solvent by rotary evaporator. The crude product was subjected into silica gel column chromatography with petroleum ether: dichloromethane (4:1, v:v) as eluent to afford IDTC5Ph as pale solids (670 mg, yield: 40%). ^{1}H NMR (400 MHz, $CDCl_3$) δ 7.27 (m, 4H), 7.19 (m, 8H), 7.11 (m, 4H), 7.02 (m, 8H), 6.93 (d, J = 4.8 Hz, 2H), 2.39 (t, J = 7.7 Hz, 8H), 2.02 – 1.90 (m, 4H), 1.89 – 1.78 (m, 4H), 1.45 – 1.35 (m, 8H), 1.17 – 1.07 (m, 8H), 0.90 – 0.77 (m, 8H). ^{13}C NMR (101 MHz, $CDCl_3$) δ 155.08, 153.27, 142.84, 141.81, 135.80, 128.50, 128.27, 126.49, 125.61, 121.76, 113.26, 53.76, 39.20, 35.86, 31.19, 29.57, 24.02.

Synthesis of IDTC5Ph-CHO: Dry DMF (1.5 mL) dissolved into 10 mL 1, 2-dichloroethane was stirred at 0 ^{o}C under argon atmosphere. After dry $POCl_3$ (2 mL) was added dropwise, the solution was stirred at 0 ^{o}C for another 1.0 hr. Then IDTC5Ph (250 mg, 0.29 mmol) dissolved into 10 mL 1,2-dichloroethane was added dropwise. Then the solution was refluxed for 48 hrs under argon protection. When the solution cooled into room temperature, it was poured into ice water and stirred for 4.0 hrs and extracted with dichloromethane (30 mL×3), dried with anhydrous Na_2SO_4, and removed the solvent by rotary evaporator. The crude product was subjected into silica gel column chromatography with petroleum ether: dichloromethane (1:2, v:v) as eluent to afford IDTC5Ph-CHO as bright yellow solids (245 mg, yield: 93%). ^{1}H NMR (600 MHz, $CDCl_3$) δ 9.91 (s, 2H), 7.61 (s, 2H), 7.45 (s, 2H), 7.20 (m, 8H), 7.14 (m, 4H), 7.03 (m, 8H), 2.42 (m, 8H), 2.02 (m, 4H), 1.93 – 1.86 (m, 4H), 1.42 (m, 8H), 1.19 – 1.13 (m, 8H), 0.88 – 0.78 (m, 8H). ^{13}C NMR (151 MHz, $CDCl_3$) δ 183.12, 156.03, 155.20, 151.44, 145.88, 142.53, 136.66, 130.46, 128.45, 128.32, 125.75, 115.17, 54.35, 38.97, 35.84, 31.14, 29.45, 24.23.

Synthesis of IDIC-C5Ph: IDTC5Ph-CHO (230 mg, 0.25 mmol) and 2-(3-oxo-2,3-dihydro-1H-inden-1-ylidene)malononitrile (291 mg, 1.5 mmol) were dissolved into 30 mL $CHCl_3$ and stirred under argon atmosphere. Then pyridine (1.0 mL) was added dropwise. Then the solution was refluxed for 24 hrs. When the solution cooled into room temperature, most of the solvent was removed. The remaining solution was precipitated into CH_3OH, filtered and the residue was washed by 100 mL CH_3OH to remove most of the end-cap compound. Then the crude product was subjected into silica gel column chromatography with dichloromethane as eluent to afford IDIC-C5Ph as deep blue solids (185 mg, yield: 59%). ^{1}H NMR (600 MHz, $CDCl_3$) δ 8.97 (s, 2H), 8.72 (d, J = 7.3 Hz, 2H), 7.97 – 7.91 (m, 2H), 7.82 – 7.75 (m, 4H), 7.72 (s, 2H), 7.58 (s, 2H), 7.19 (m, 8H), 7.10 (m, 4H), 7.03 (m, 8H), 2.43 (m, 8H), 2.09 – 2.01 (m, 4H), 1.93 (m, 4H), 1.47 – 1.40 (m, 8H), 1.22 – 1.15 (m, 8H), 0.94 – 0.80 (m, 8H). ^{13}C NMR (151 MHz, $CDCl_3$) δ 188.42, 160.79, 160.07, 157.44, 156.61, 142.53, 141.32, 140.11, 138.55, 138.04, 137.76, 137.10, 135.29, 134.63, 128.46, 128.32, 125.72, 125.47, 123.91, 122.37, 116.13, 114.91, 114.85, 69.21, 54.40, 39.08, 35.88, 31.13, 29.51, 24.36. Elemental Analysis: C, 82.00; H, 5.92; N, 4.45; S, 5.09. found: C, 81.89; H, 5.91; N, 4.56; S, 5.37.

Synthesis of IDTC6Ph: IDT (500 mg, 1.88 mmol) was dispersed in 15 mL dry DMSO and stirred under argon atmosphere. Then ^{t}BuOK (1.26 g, 11.3 mmol) was added in small portions. After then, the solution was heated at 80 ^{o}C for 1.0 hr. Subsequently, (6-bromohexyl)benzene (3.60 g, 1.84 mL, 15.0 mmol) was dropwise added into the solution and heated at 85-90 ^{o}C for another 5.0 hrs. When the solution cooled into room

temperature, it was poured into ice water and extracted with dichloromethane (50 mL×3), dried with anhydrous Na_2SO_4, and removed the solvent by rotary evaporator. The crude product was subjected into silica gel column chromatography with petroleum ether: dichloromethane (4:1, v:v) as eluent to afford IDTC6Ph as pale solids (710 mg, yield: 42%). ^{1}H NMR (600 MHz, $CDCl_3$) δ 7.28 – 7.24 (m, 4H), 7.21 (m, 8H), 7.12 (m, 4H), 7.08 (m, 8H), 6.94 (d, *J* = 4.8 Hz, 2H), 2.50 – 2.44 (m, 8H), 1.99 – 1.91 (m, 4H), 1.86 – 1.79 (m, 4H), 1.46 – 1.41 (m, 8H), 1.13 (br, 16H), 0.87 – 0.81 (m, 8H). ^{13}C NMR (151 MHz, $CDCl_3$) δ 155.17, 153.36, 142.98, 141.77, 135.69, 128.50, 128.30, 126.39, 125.63, 121.86, 113.28, 53.74, 39.21, 36.01, 31.53, 29.94, 29.09, 24.22.

Synthesis of IDTC6Ph-CHO: Dry DMF (1.5 mL) dissolved into 10 mL 1, 2-dichloroethane was stirred at 0 ^{o}C under argon atmosphere. After dry $POCl_3$ (2 mL) was added dropwise, the solution was stirred at 0 ^{o}C for another 1.0 hr. Then IDTC6Ph (250 mg, 0.27 mmol) dissolved into 10 mL 1,2-dichloroethane was added dropwise. Then the solution was refluxed for 48 hrs under argon protection. When the solution cooled into room temperature, it was poured into ice water and stirred for 4.0 hrs and extracted with dichloromethane (30 mL×3), dried with anhydrous Na_2SO_4, and removed the solvent by rotary evaporator. The crude product was subjected into silica gel column chromatography with petroleum ether: dichloromethane (1:2, v:v) as eluent to afford IDTC6Ph-CHO as bright yellow solids (215 mg, yield: 83%). ^{1}H NMR (600 MHz, $CDCl_3$) δ 9.91 (s, 2H), 7.62 (s, 2H), 7.45 (s, 2H), 7.22 (m, 8H), 7.14 (m, 4H), 7.09 (m, 8H), 2.53 – 2.47 (m, 8H), 2.02 (m, 4H), 1.88 (m, 4H), 1.46 (m, 8H), 1.15 (br, 16H), 0.83 (m, 8H). ^{13}C NMR (151 MHz, $CDCl_3$) δ 183.13, 156.12, 155.29, 151.47, 145.81, 142.76, 136.57, 130.52, 128.45, 128.35, 125.74, 115.20, 54.33, 38.96, 35.96, 31.45, 29.85, 29.02, 24.37.

Synthesis of IDIC-C6Ph: IDTC6Ph-CHO (205 mg, 0.21 mmol) and 2-(3-oxo-2,3-dihydro-1H-inden-1-ylidene)malononitrile (248 mg, 1.2 mmol) were dissolved into 30 mL $CHCl_3$ and stirred under argon atmosphere. Then pyridine (1.0 mL) was added dropwise. After then , the solution was refluxed for 24 hrs. When the solution cooled into room temperature, most of the solvent was removed. The remaining solution was precipitated into CH_3OH, filtered and the residue was washed by 100 mL CH_3OH to remove most of the end-cap compound. Then the crude product was subjected into silica gel column chromatography with dichloromethane as eluent to afford IDIC-C6Ph as deep blue solids (220 mg, yield: 80%). ^{1}H NMR (600 MHz, $CDCl_3$) δ 8.97 (s, 2H), 8.71 (d, *J* = 7.5 Hz, 2H), 7.98 – 7.93 (m, 2H), 7.82 – 7.74 (m, 4H), 7.72 (s, 2H), 7.58 (s, 2H), 7.20 (m, 8H), 7.10 (m, 12H), 2.52 – 2.47 (m, 8H), 2.08 – 2.00 (m, 4H), 1.95 – 1.88 (m, 4H), 1.50 – 1.44 (m, 8H), 1.17 (s, 16H), 0.94 – 0.79 (m, 8H). ^{13}C NMR (151 MHz, $CDCl_3$) δ 188.45, 160.80, 160.16, 157.53, 156.70, 142.79, 141.30, 140.11, 138.58, 137.99, 137.88, 137.09, 135.28, 134.62, 128.46, 128.32, 125.68, 125.46, 123.90, 122.30, 116.17, 114.93, 114.86, 69.15, 54.39, 39.06, 35.97, 31.48, 29.86, 29.05, 24.47. Elemental Analysis: C, 82.16; H, 6.28; N, 4.26; S, 4.87. found: C, 82.03; H, 6.25; N, 4.30; S, 4.99.

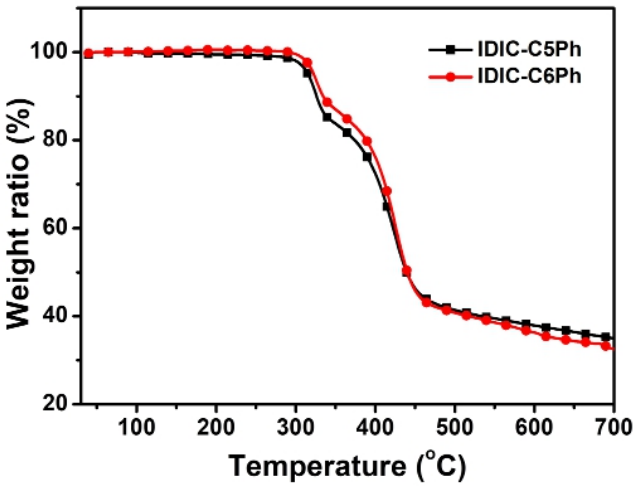

Figure. S1 TGA curves with a heating rate of 10 °C/min in N_2 atmosphere.

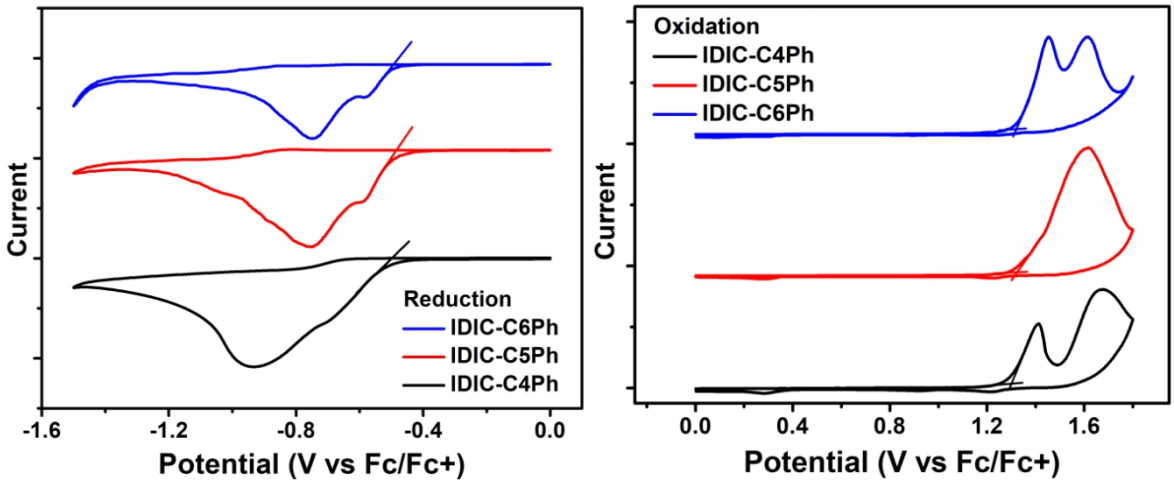

Figure S2. The cyclic voltammogram curves of IDIC-CxPh (x=4, 5, 6) on glassy carbon electrodes in 0.1 M Bu_4NPF_6-CH_3CN at a scan rate of 100 mV s^{-1}.

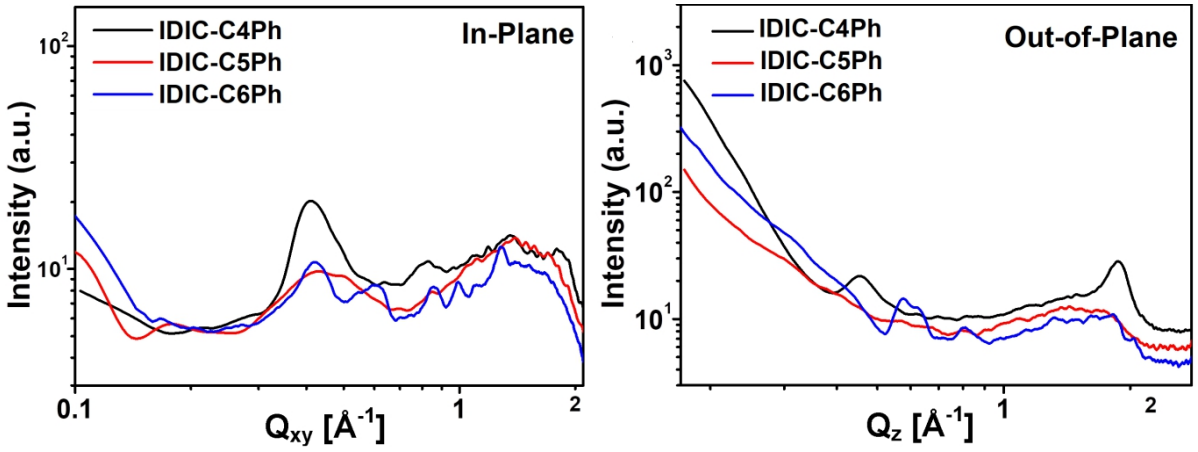

Figure S3. The line profiles of GIWAXS of IDIC-CxPh (x=4, 5, 6) films.

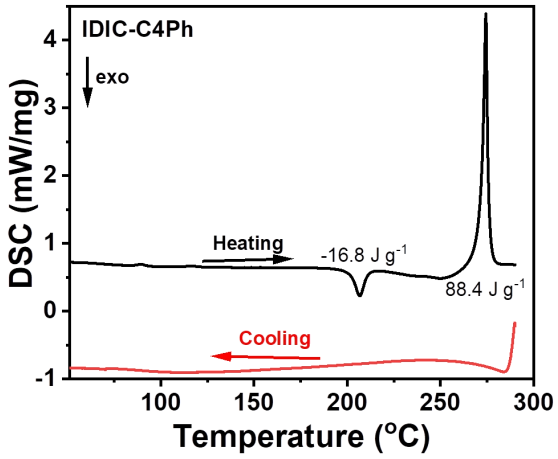

Figure S4. The DSC curves of IDIC-C4Ph powder with a heating rate of 10 °C/min in N_2 atmosphere.

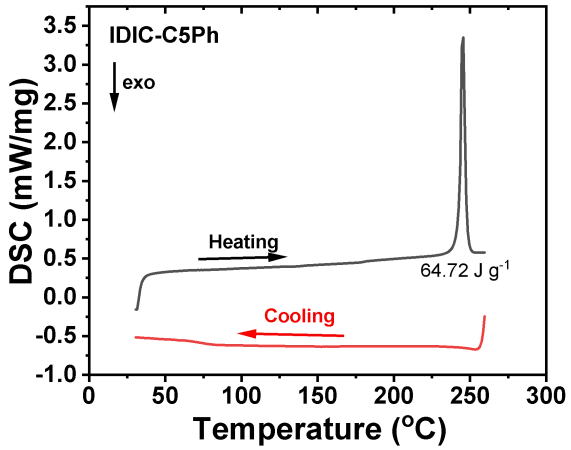

Figure S5. The DSC curves of IDIC-C5Ph powder with a heating rate of 10 °C/min in N_2 atmosphere.

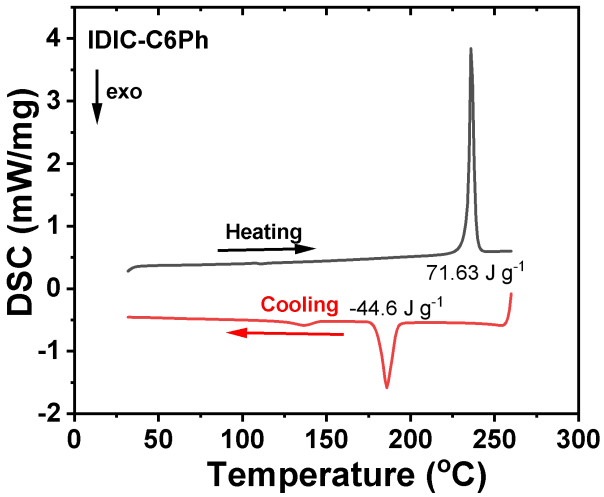

Figure S6. The DSC curves of IDIC-C6Ph powder with a heating rate of 10 °C/min in N_2 atmosphere.

Table S1. Crystal data and structure refinement for IDIC-C4Ph

CCDC number	1947277	
Identification code	IDIC-C4Ph	
Empirical formula	$C_{82}H_{66}N_4O_2S_2$	
Formula weight	1203.50	
Temperature	293(2) K	
Wavelength	1.54184 Å	
Crystal system	Monoclinic	
Space group	P 1 21/n 1	
Unit cell dimensions	a = 16.1333(4) Å	a= 90°.
	b = 21.4697(5) Å	b= 112.268(3)°.
	c = 20.8049(4) Å	g = 90°.
Volume	6668.9(3) $Å^3$	
Z	4	
Density (calculated)[a]	1.199 g cm^{-3}	
Absorption coefficient	1.119 mm^{-1}	
F(000)	2536	
Crystal size	0.2 x 0.15 x 0.1 mm^3	
Theta range for data collection	2.980 to 75.447°.	
Index ranges	-20<=h<=19, -25<=k<=26, -22<=l<=26	
Reflections collected	46993	
Independent reflections	13202 [R(int) = 0.0539]	
Completeness to theta = 67.684°	99.8 %	
Absorption correction	Semi-empirical from equivalents	
Max. and min. transmission	1.00000 and 0.58177	
Refinement method	Full-matrix least-squares on F^2	
Data / restraints / parameters	13202 / 790 / 1001	
Goodness-of-fit on F^2	1.427	
Final R indices [I>2sigma(I)]	R1 = 0.1109, wR2 = 0.3353	
R indices (all data)	R1 = 0.1381, wR2 = 0.3665	
Extinction coefficient	n/a	
Largest diff. peak and hole	1.328 and -0.498 e.$Å^{-3}$	

[a] The densities of the single crystals are automatically calculated from the SHELXL software based on the cell volume, Z value and molecular formula parameters.

Table S2. Crystal data and structure refinement for IDIC-C5Ph

CCDC number	1947278	
Identification code	IDIC-C5Ph	
Empirical formula	$C_{86}H_{74}N_4O_2S_2$	
Formula weight	1259.68	
Temperature	293(2) K	
Wavelength	1.54178 Å	
Crystal system	Triclinic	
Space group	P -1	
Unit cell dimensions	a = 15.08430(10) Å	a= 102.8640(10)°.
	b = 15.2016(2) Å	b= 95.0000(10)°.
	c = 16.6580(2) Å	g = 98.3670(10)°.
Volume	3655.85(7) $Å^3$	
Z	2	
Density (calculated) [a]	1.253 g cm-3	
Absorption coefficient	2.070 mm^{-1}	
F(000)	1448	
Crystal size	0.35 x 0.2 x 0.15 mm^3	
Theta range for data collection	2.742 to 75.355°.	
Index ranges	-18<=h<=18, -18<=k<=18, -20<=l<=11	
Reflections collected	31563	
Independent reflections	13149 [R(int) = 0.0195]	
Completeness to theta = 67.684°	93.2 %	
Absorption correction	Semi-empirical from equivalents	
Max. and min. transmission	1.000 and 0.7273	
Refinement method	Full-matrix least-squares on F^2	
Data / restraints / parameters	13149 / 108 / 920	
Goodness-of-fit on F^2	1.086	
Final R indices [I>2sigma(I)]	R1 = 0.0521, wR2 = 0.1342	
R indices (all data)	R1 = 0.0592, wR2 = 0.1516	
Extinction coefficient	n/a	
Largest diff. peak and hole	1.132 and -0.613 e.$Å^{-3}$	

[a] The densities of the single crystals are automatically calculated from the SHELXL software based on the cell volume, Z value and molecular formula parameters.

Table S3. Crystal data and structure refinement for IDIC-C6Ph

CCDC number	1947279	
Identification code	IDIC-C6Ph	
Empirical formula	$C_{90}H_{82}N_4O_2S_2$	
Formula weight	1315.79	
Temperature	293(2) K	
Wavelength	1.54178 Å	
Crystal system	Triclinic	
Space group	P -1	
Unit cell dimensions	a = 14.9275(3) Å	a= 82.8460(10)°.
	b = 15.8487(2) Å	b= 89.0300(10)°.
	c = 35.0092(5) Å	g = 76.3500(10)°.
Volume	7985.3(2) $Å^3$	
Z	4	
Density (calculated) [a]	1.194 g cm-3	
Absorption coefficient	1.913 mm^{-1}	
F(000)	3024	
Crystal size	0.6 x 0.35 x 0.07 mm^3	
Theta range for data collection	2.544 to 75.677°.	
Index ranges	-18<=h<=18, -19<=k<=19, -43<=l<=43	
Reflections collected	31663	
Independent reflections	31663 [R(int) = 0.052]	
Completeness to theta = 67.684°	99.8 %	
Absorption correction	Semi-empirical from equivalents	
Max. and min. transmission	1.0000 and 0.81573	
Refinement method	Full-matrix least-squares on F^2	
Data / restraints / parameters	31663 / 124 / 1875	
Goodness-of-fit on F^2	1.037	
Final R indices [I>2sigma(I)]	R1 = 0.0896, wR2 = 0.2637	
R indices (all data)	R1 = 0.1046, wR2 = 0.2785	
Extinction coefficient	n/a	
Largest diff. peak and hole	1.379 and -0.840 e.$Å^{-3}$	

[a] The densities of the single crystals are automatically calculated from the SHELXL software based on the cell volume, Z value and molecular formula parameters.

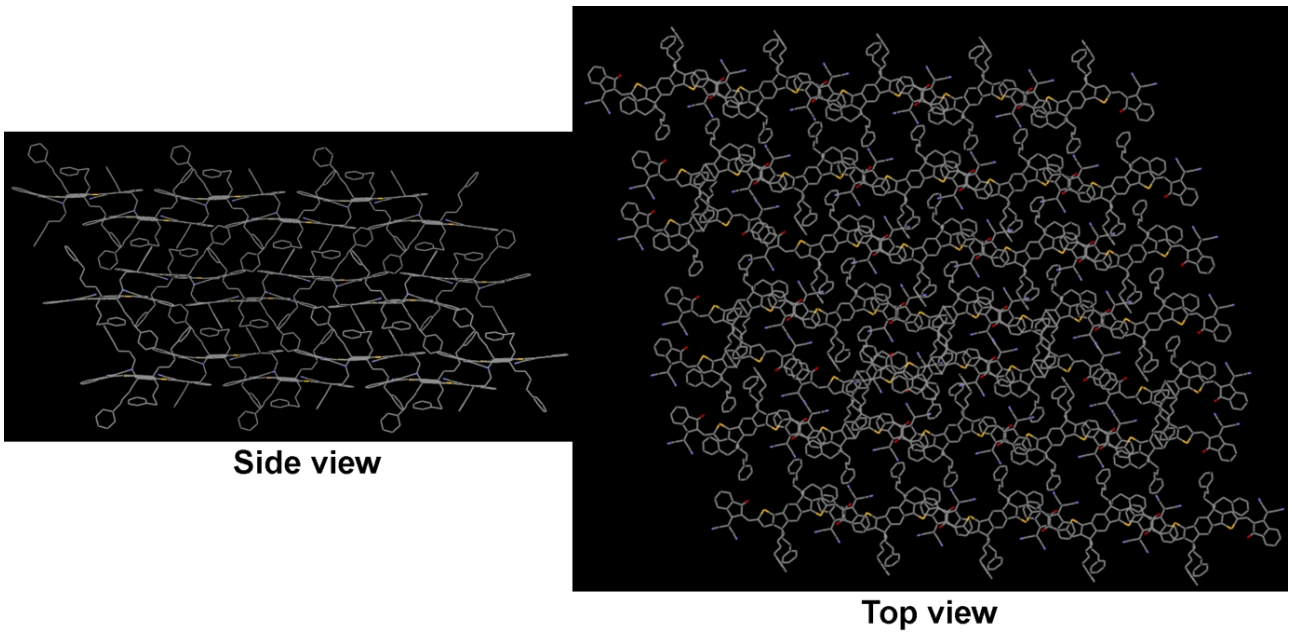

Figure S7. The molecular assembly in IDIC-C4Ph single crystal (H atoms are hidden).

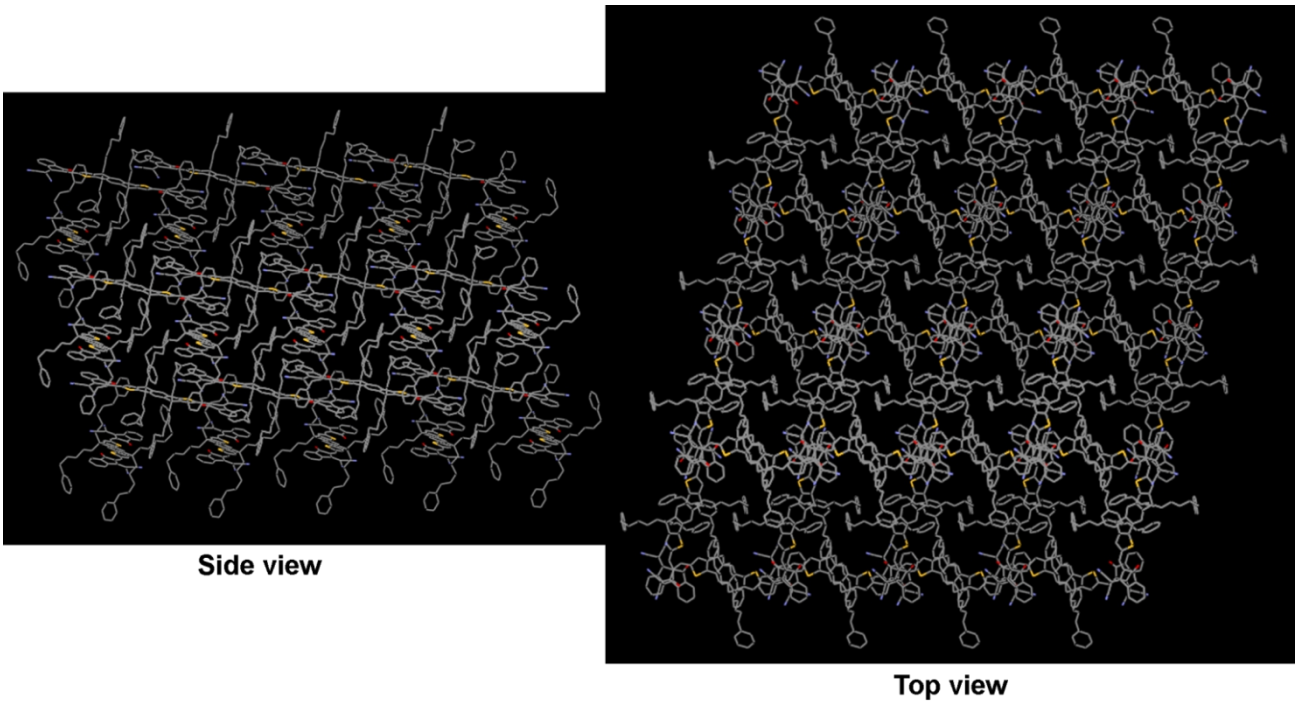

Figure S8. The molecular assembly in IDIC-C5Ph single crystal (H atoms are hidden; top view).

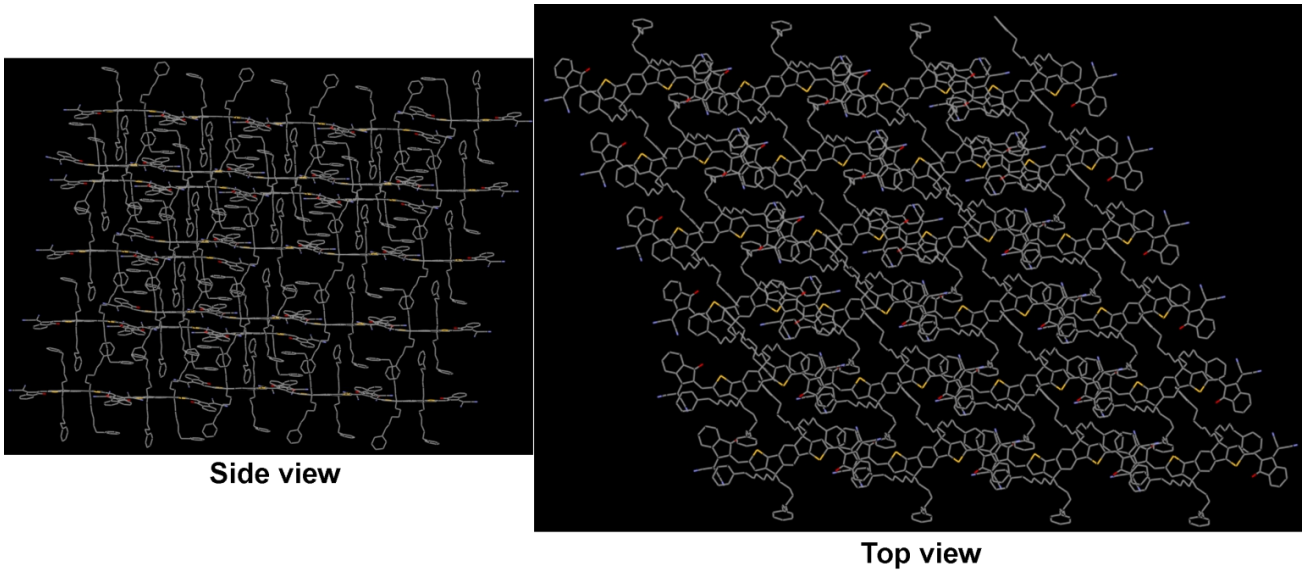

Figure S9. The molecular assembly in IDIC-C6Ph single crystal (H atoms are hidden).

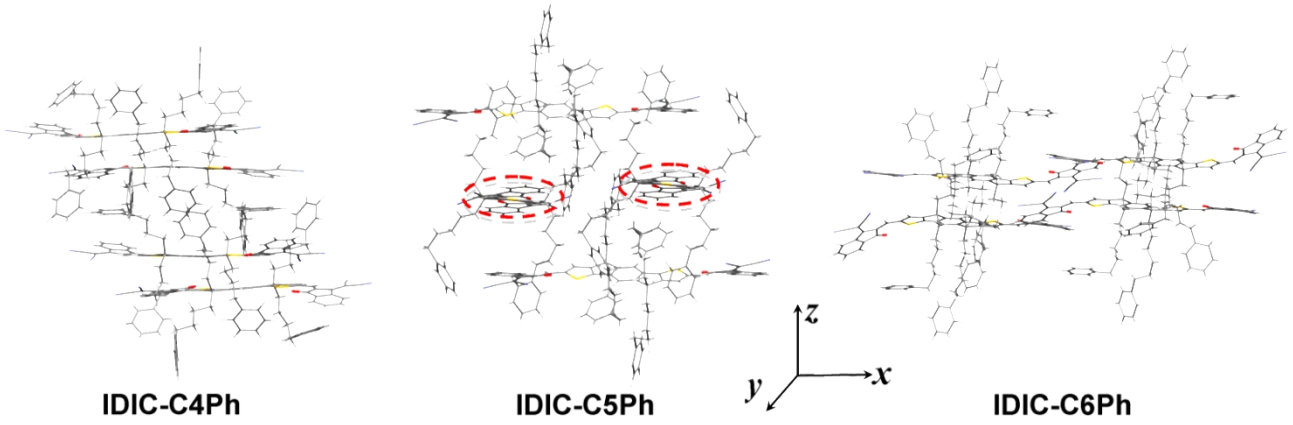

Figure S10. The molecular conformations and stacking of IDIC-CxPh (x=4, 5 and 6) based on DFT calculations with B3LYP-D3/def2-SVP algorithm.

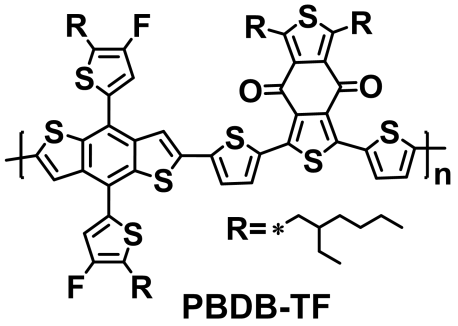

Figure S11. The chemical structure of polymer donor PBDB-TF used in this work.

Table S4. The photovoltaic parameters of as-cast OSCs with different donor/acceptor weight ratios under the illumination of AM 1.5G, 100 mW cm^{-2}

Acceptor	*Donor/acceptor*	V_{OC}	J_{SC}	FF	PCE
	w/w	(V)	(mA cm^{-2})	(%)	(%)[a]
IDIC-C4Ph	1:0.8	0.950	17.24	75.72	12.40 (12.14)
	1:1	0.952	18.06	76.77	13.20 (13.00)
	1:1.5	0.954	17.80	74.37	12.63 (12.32)
IDIC-C5Ph	1:0.8	0.956	17.69	69.33	11.72 (11.48)
	1:1	0.961	18.25	71.37	12.52 (12.24)
	1:1.5	0.963	18.02	70.11	12.17 (11.95)
IDIC-C6Ph	1:0.8	0.940	15.12	62.81	8.93 (8.77)
	1:1	0.949	16.03	66.68	10.14 (9.87)
	1:1.5	0.956	15.41	62.30	9.18 (9.00)

[a] The PCEs in brackets represent the average values based on at least 10 devices.

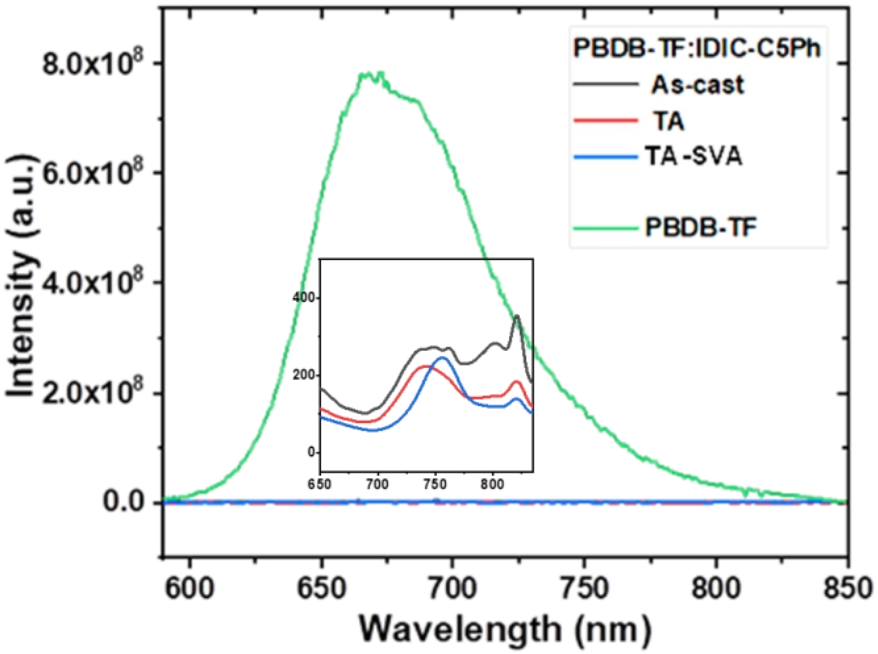

Figure S12. The PL spectra of neat PBDB-TF, BHJ blends under different conditions (excited at 580 nm). The inset is the enlarged PL spectra of blends.

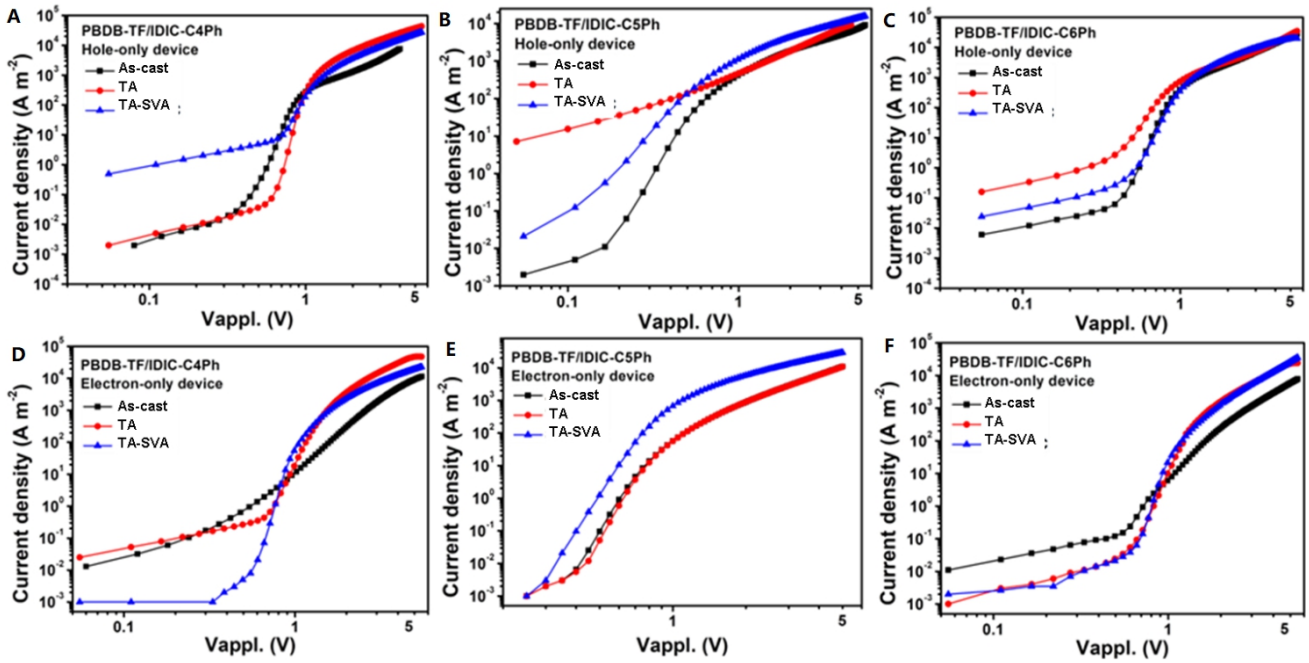

Figure S13. (A-C) The hole mobility and (D-F) electron mobility of OSCs with BHJsunder different conditions.

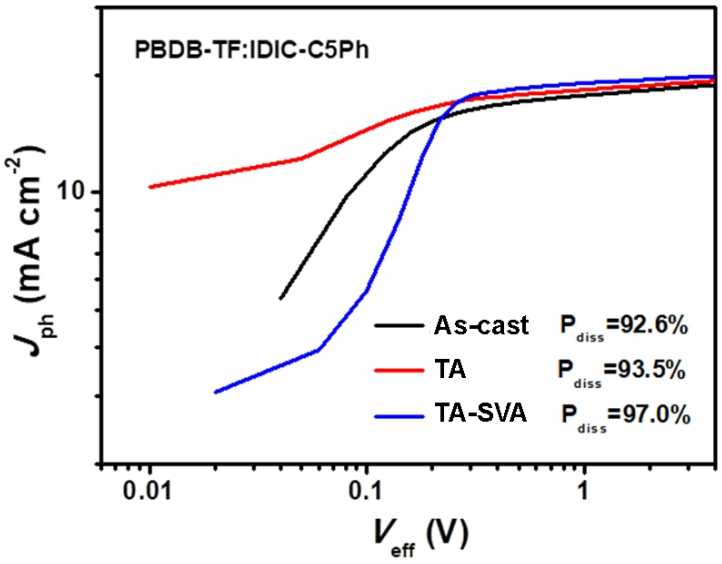

Figure S14. Photocurrent density (J_{ph}) plotted with respect to the effective bias (V_{eff}) for PBDB-TF:IDIC-C5Ph devices under different treatments.

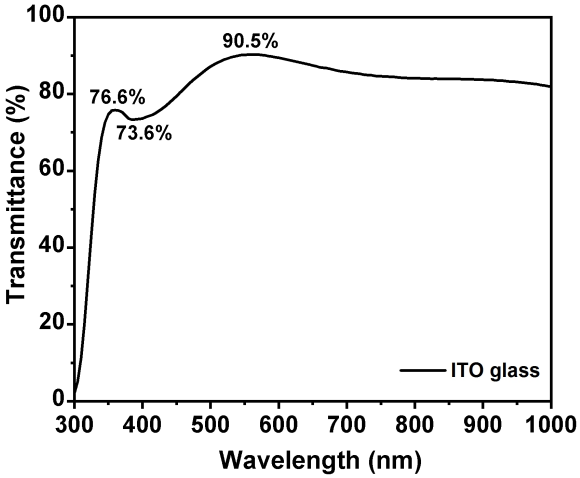

Figure S15. The transmittance curve of ITO glass.

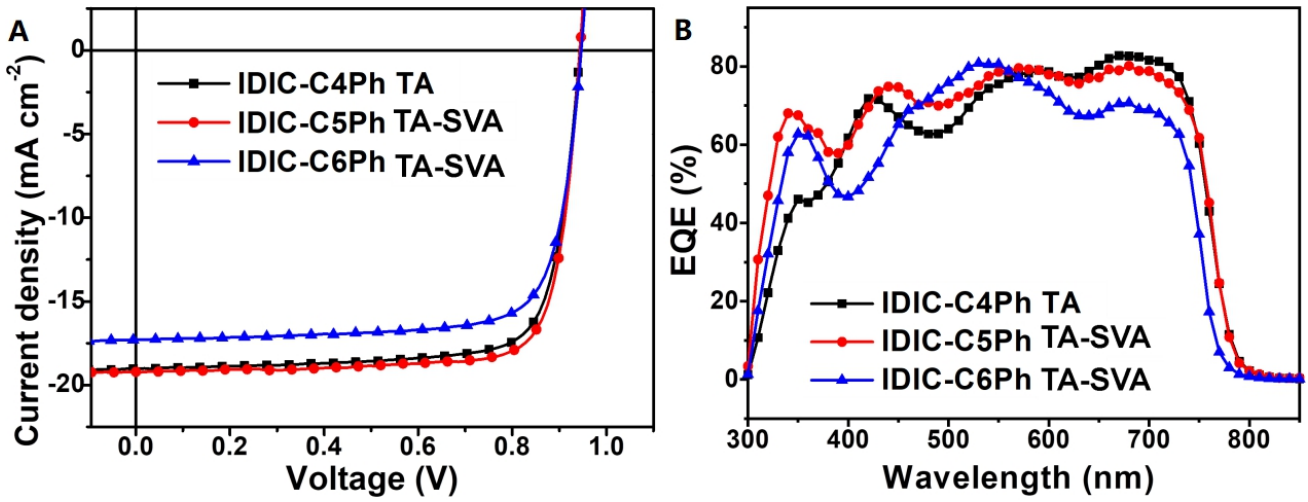

Figure S16. (A) The *J-V* curves of three optimized OSCs and (B) corresponding EQE curves.

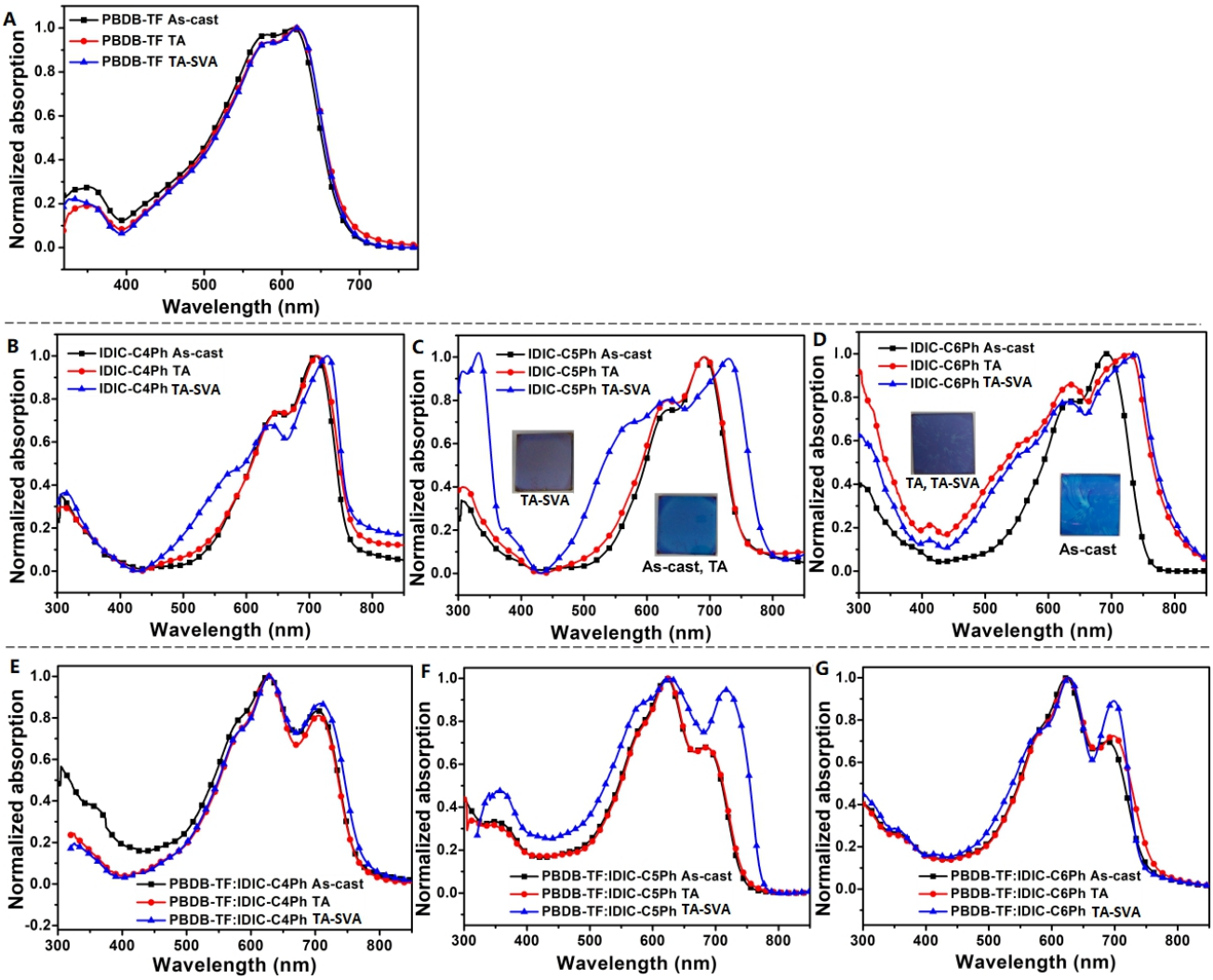

Figure S17. The absorption spectra of polymer PBDB-TF, three neat acceptors and respective blend films under different post-treatments.

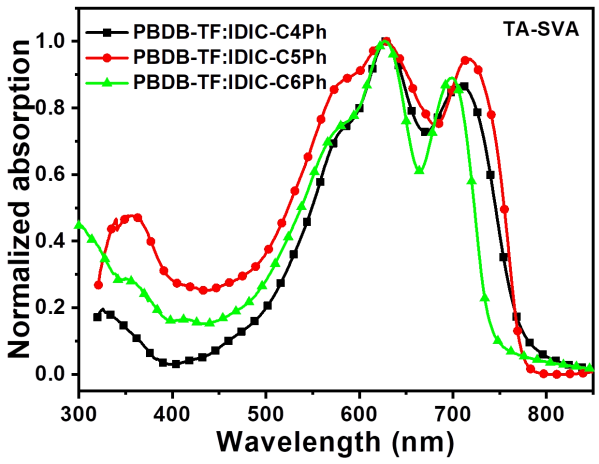

Figure S18. The absorption spectra of three BHJ blends under TA-SVA treatments.

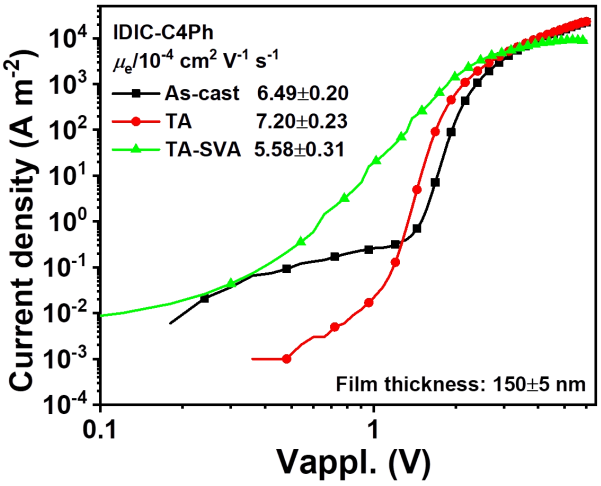

Figure S19. The SCLC curves and electron mobilities of pure acceptor IDIC-C4Ph under different treatments.

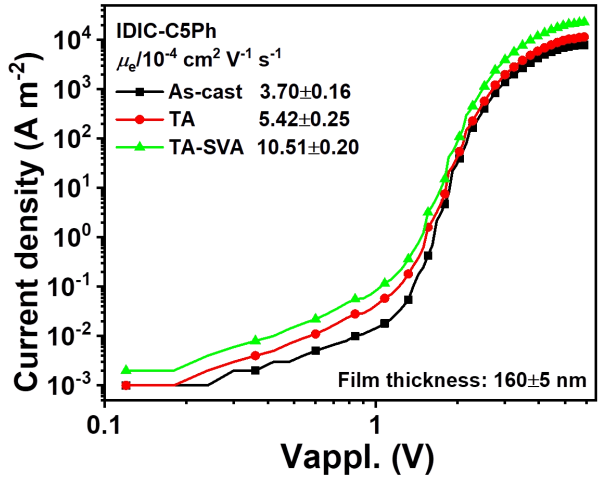

Figure S20. The SCLC curves and electron mobilities of pure acceptor IDIC-C5Ph under different treatments.

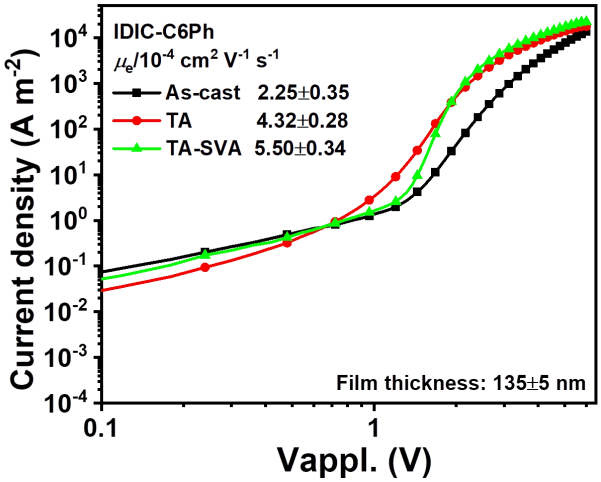

Figure S21. The SCLC curves and electron mobilities of pure acceptor IDIC-C6Ph under different treatments.

Table S5. The q locations and π-π-stacking distances in OOP direction of GIWAXS studies

Blend		q (Å^{-1})	$d_{spacing}$π-π (Å)
PBDB-TF:	As-cast	1.78	3.53
	TA	1.83	3.44
IDIC-C4Ph	TA-SVA	1.78	3.53
PBDB-TF:	As-cast	1.76	3.58
	TA	1.76	3.58
IDIC-C5Ph	TA-SVA	1.88	3.34
PBDB-TF:	As-cast	1.76	3.58
	TA	1.80	3.48
IDIC-C6Ph	TA-SVA	1.80	3.48

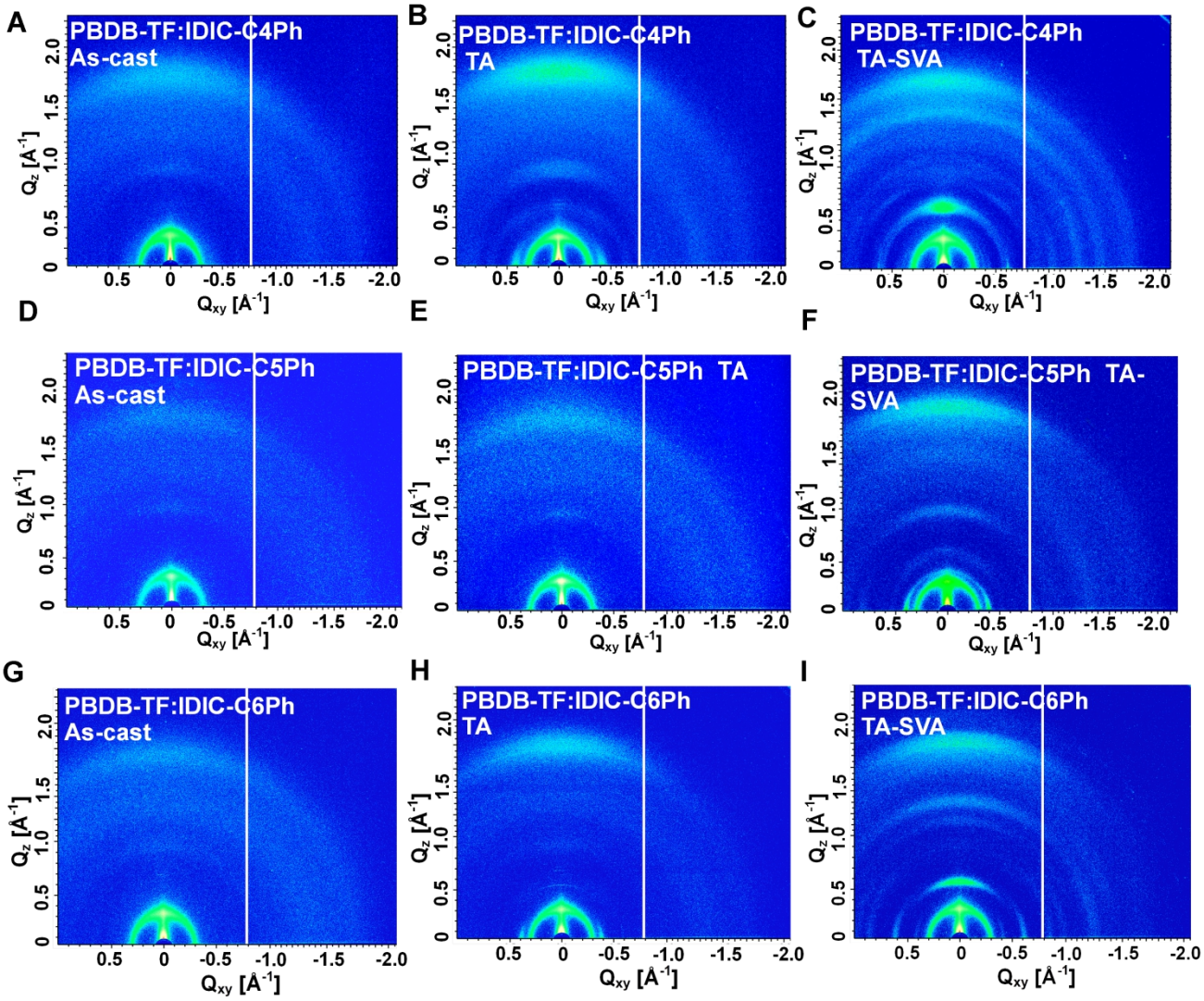

Figure S22. The 2D-GIWAXS images of PBDB-TF:IDIC-C4Ph (A-C), PBDB-TF:IDIC-C5Ph (D-F) and PBDB-TF:IDIC-C6Ph (G-I) under different treatments.

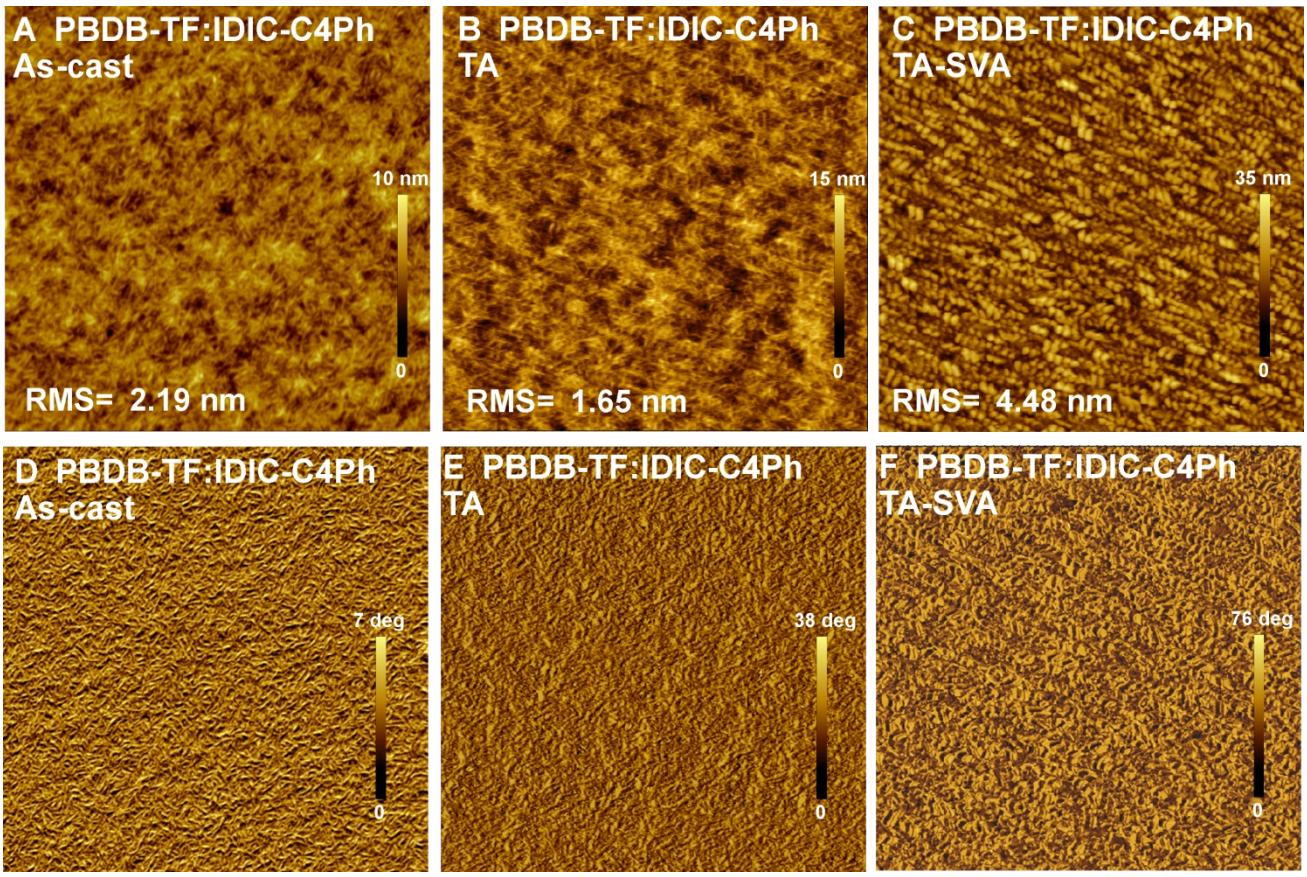

Figure S23. (A-C) The AFM and (D-F) phase images of PBDB-TF:IDIC-C4Ph under different treatments.

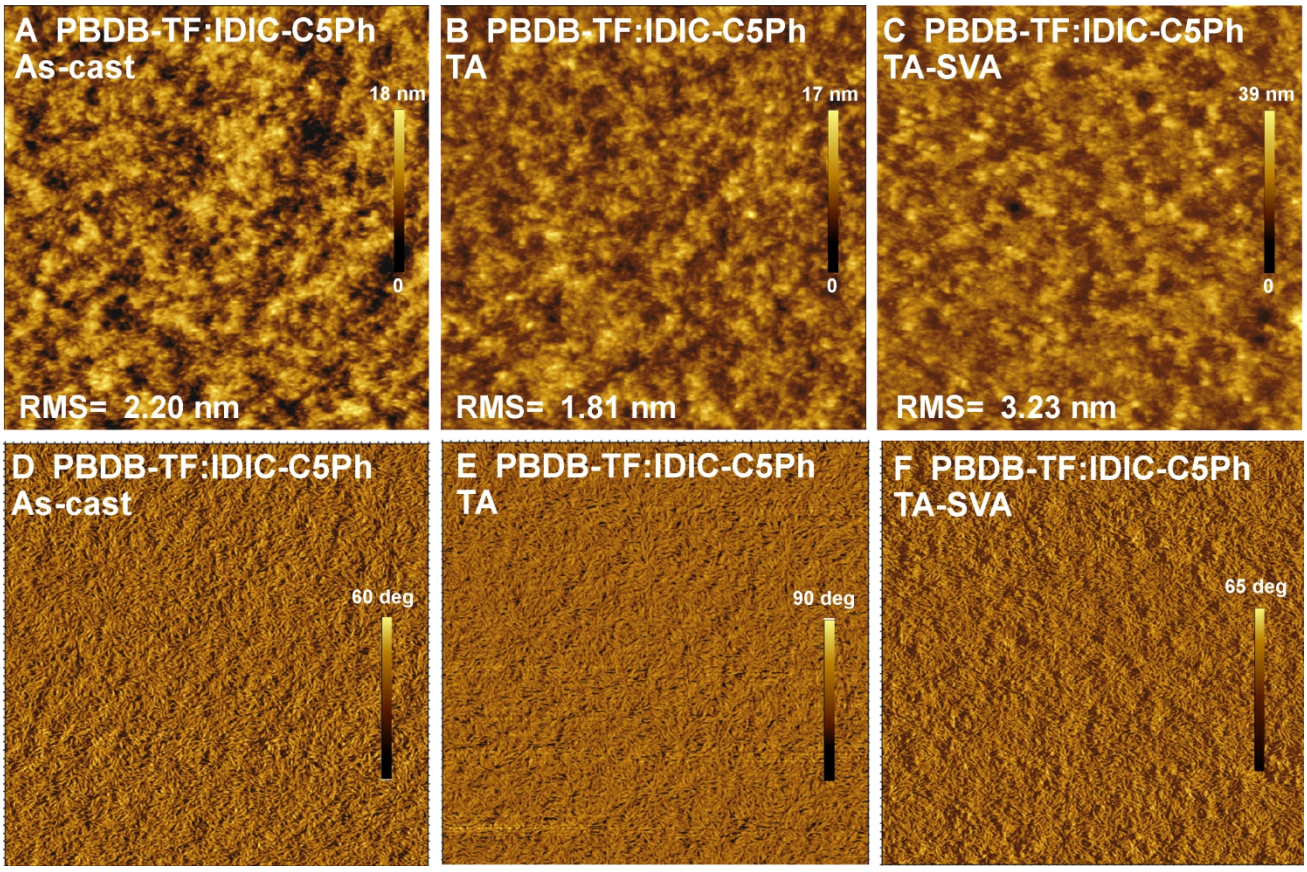

Figure S24. (A-C) The AFM and (D-F) phase images of PBDB-TF:IDIC-C5Ph under different treatments.

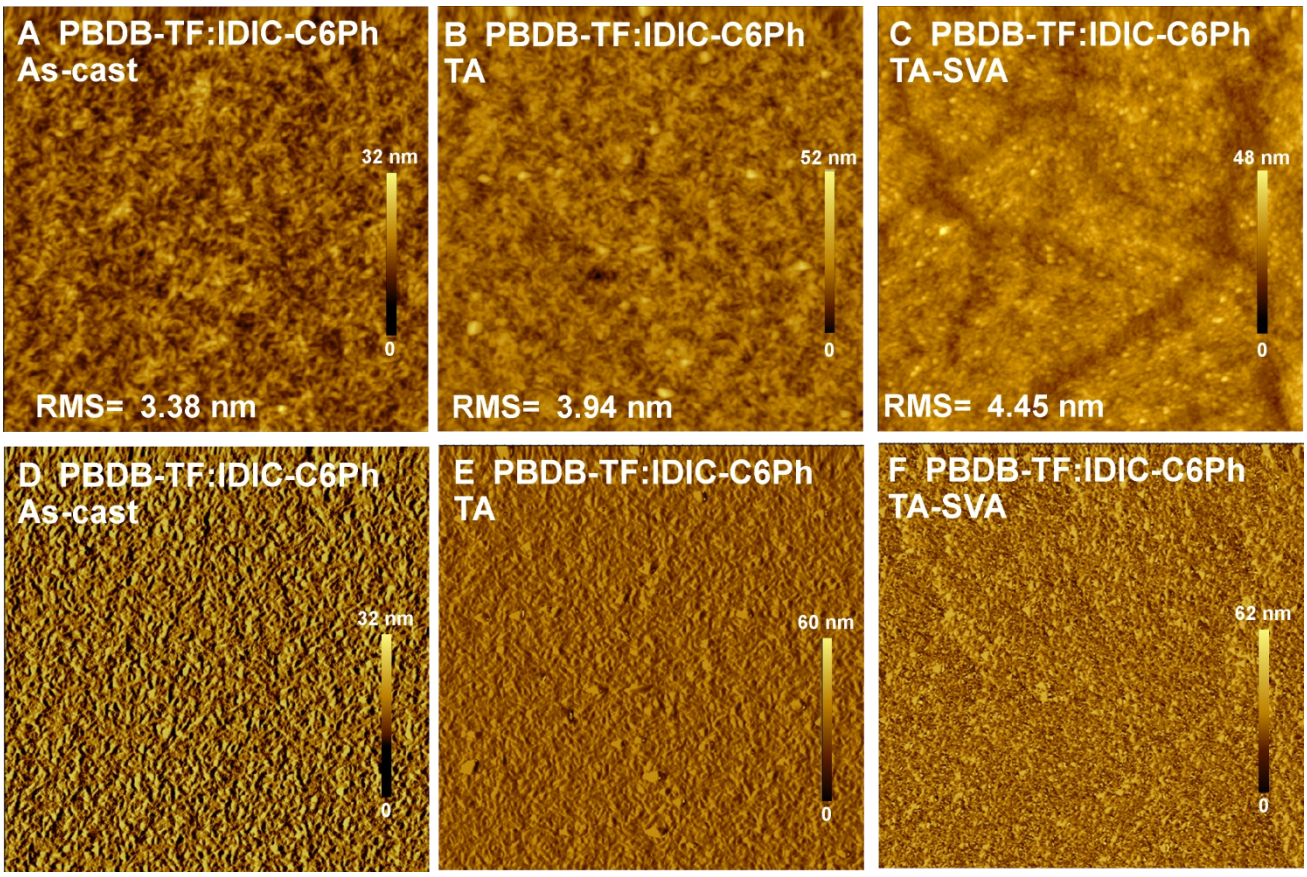

Figure S25. (A-C) The AFM and (D-F) phase images of PBDB-TF:IDIC-C6Ph under different treatments.

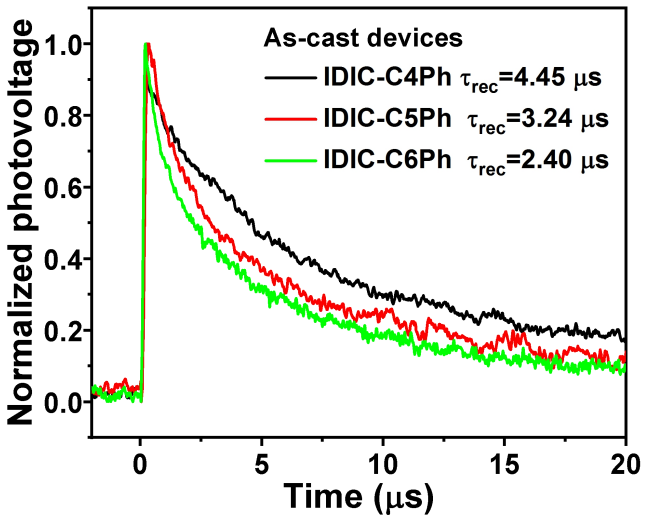

Figure S26. The transient photovoltage (TPV) decay kinetics of three as-cast devices.

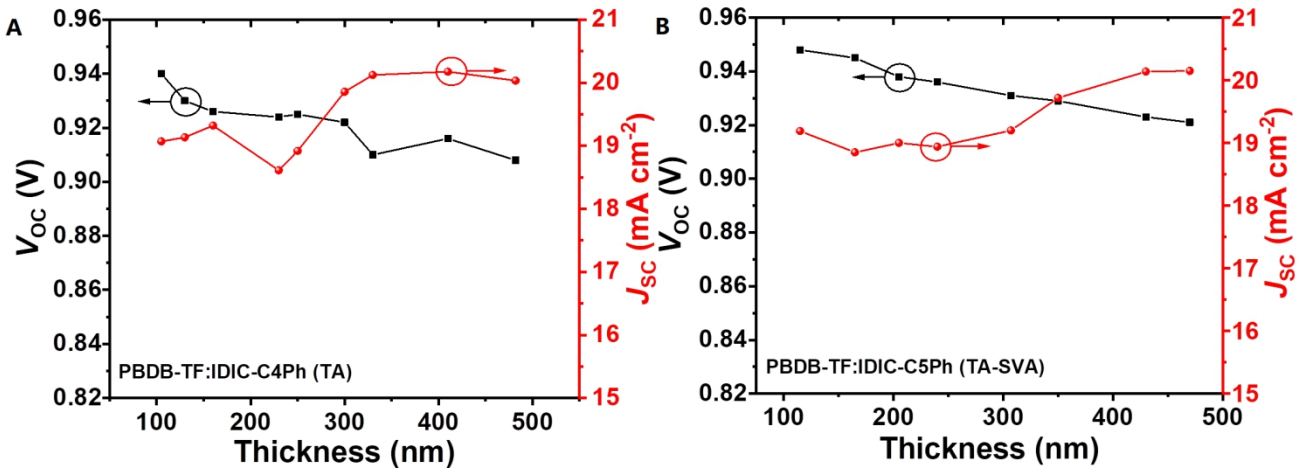

Figure S27. The V_{OC} and J_{SC} of the optimal solar cells (A) PBDB-TF:IDIC-C4Ph and (B) PBDB-TF:IDIC-C5Ph *versus* the active layer film thickness.

Table S6. The photovoltaic performance of PBDB-TF:IDIC-C4Ph (TA) and PBDB-TF:IDIC-C5Ph (TA-SVA) based thick-film OSCs

Blend	Film thickness	V_{OC}	J_{SC}	FF	PCE
	nm	(V)	(mA cm^{-2})	(%)	(%)[a]
PBDB-TF:IDIC-C4Ph	482	0.908	20.03	65.26	11.87
	410	0.916	20.17	68.31	12.62
	330	0.910	19.90	71.35	12.92
	300	0.922	19.85	70.20	12.86
	250	0.925	18.92	74.53	13.02
	230	0.924	18.61	76.49	13.16
	160	0.926	19.32	75.21	13.50
	130	0.930	19.13	78.02	13.88
	105	0.942	18.96	78.05	13.94
PBDB-TF:IDIC-C5Ph	470	0.921	20.15	70.12	13.01
	430	0.923	20.14	72.03	13.39
	350	0.929	19.72	73.75	13.51
	307	0.931	19.20	75.51	13.49
	240	0.936	18.94	78.76	13.96
	205	0.938	19.01	79.02	14.08
	165	0.945	18.85	79.71	14.20
	115	0.948	19.19	80.02	14.56

The film thickness were controlled by changing the total concentration of donor/acceptor (18 mg ml^{-1} to 40 mg ml^{-1}), and the spin-coating speed (500 rpm to 4000 rpm).

Table S7. The photovoltaic performance of thick-film OSCs

	Active layer	Film thickness (nm)	V_{OC} (V)	J_{SC} (mA cm^{-2})	FF (%)	PCE (%)	Ref.
1	PBDB-TF:	300	0.922	19.85	70.20	12.86	This work
2	IDIC-C4Ph	482	0.908	20.03	65.26	11.87	This work
3		**307**	**0.931**	**19.20**	**75.51**	**13.49**	This work
4	PBDB-TF:	350	0.929	19.72	73.75	13.51	This work
5	IDIC-C5Ph	430	0.923	20.14	72.03	13.39	This work
6		**470**	**0.921**	**20.15**	**70.12**	**13.01**	This work
7	PM7:MF1	312	0.934	17.21	74.9	12.03	S1
8		445	0.931	17.06	69.9	11.11	S1
9		308	0.952	19.54	66.1	12.34	S1
10	PM7:MF2	438	0.955	19.35	59.8	11.04	S1
11		500	0.953	19.20	54.9	10.04	S1
12	PBDB-T: IDT-OB	320	0.87	16.34	60.0	8.57	S2
13		420	0.86	17.00	50.2	7.39	S2
14		500	0.84	17.23	47.9	6.93	S2
15	PBDB-TF:IDTN	380	0.91	17.86	58.0	9.40	S3
16		315	0.92	18.11	64.1	10.6	S4
17	PTQ10:IDTPC	400	0.91	17.90	61.3	10.0	S4
18		505	0.91	17.81	56.9	9.2	S4
19	PTQ10:IDIC	310	0.94	19.16	57.1	10.3	S5
20	J61:m-ITIC	360	0.882	19.04	49.36	8.34	S6
21	PBDB-T: m-ITIC-O-EH	302	0.86	15.58	54	7.32	S7
22	PM6:Y6	300	0.823	26.5	62.3	13.6	S8
23	PffBT4T-2OD: PC61BM	300	0.78	17.5	75	10.2	S9
24	PNT4T-2OD: PC71BM	300	0.76	19.8	68	10.1	S9
25	PPDT2FBT: PC71BM	290	0.79	16.3	73	9.39	S10
26	DT-PDPP2T-TT: PC71BM	340	0.67	20.1	70	9.4	S11
27	BTR:PC71BM	330	0.89	12.71	69	7.9	S12
28		400	0.88	12.71	68	7.6	S12

NMR spectra (Figures S27-S40)

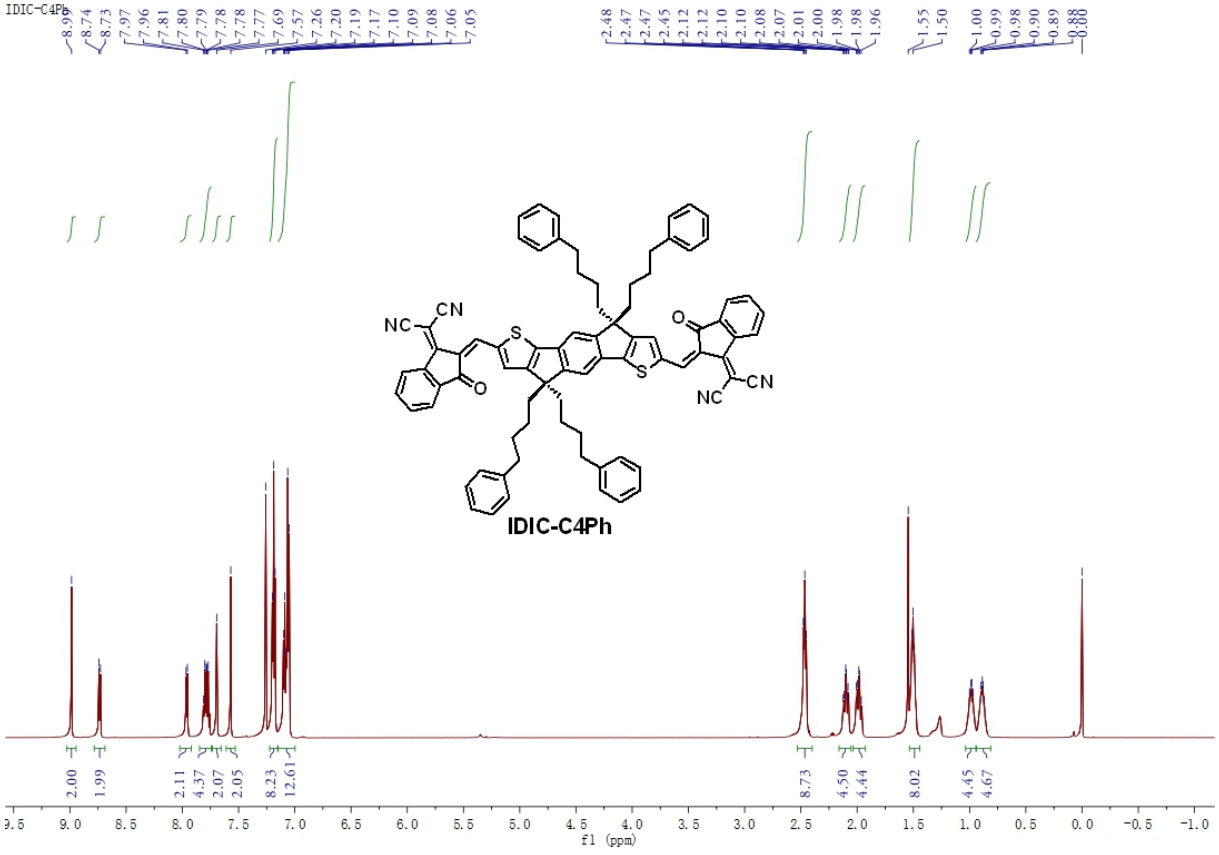

The ^{1}H NMR spectrum of IDIC-C4Ph.

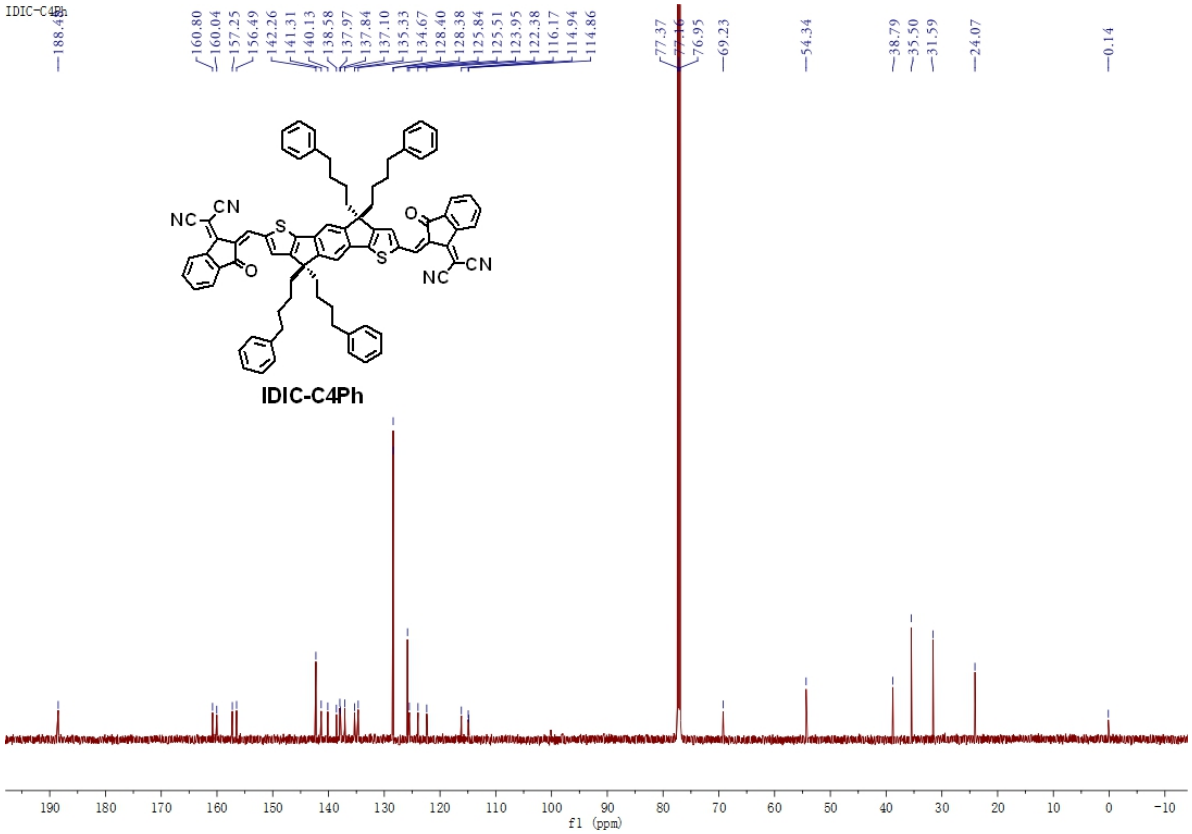

The ^{13}C NMR spectrum of IDIC-C4Ph.

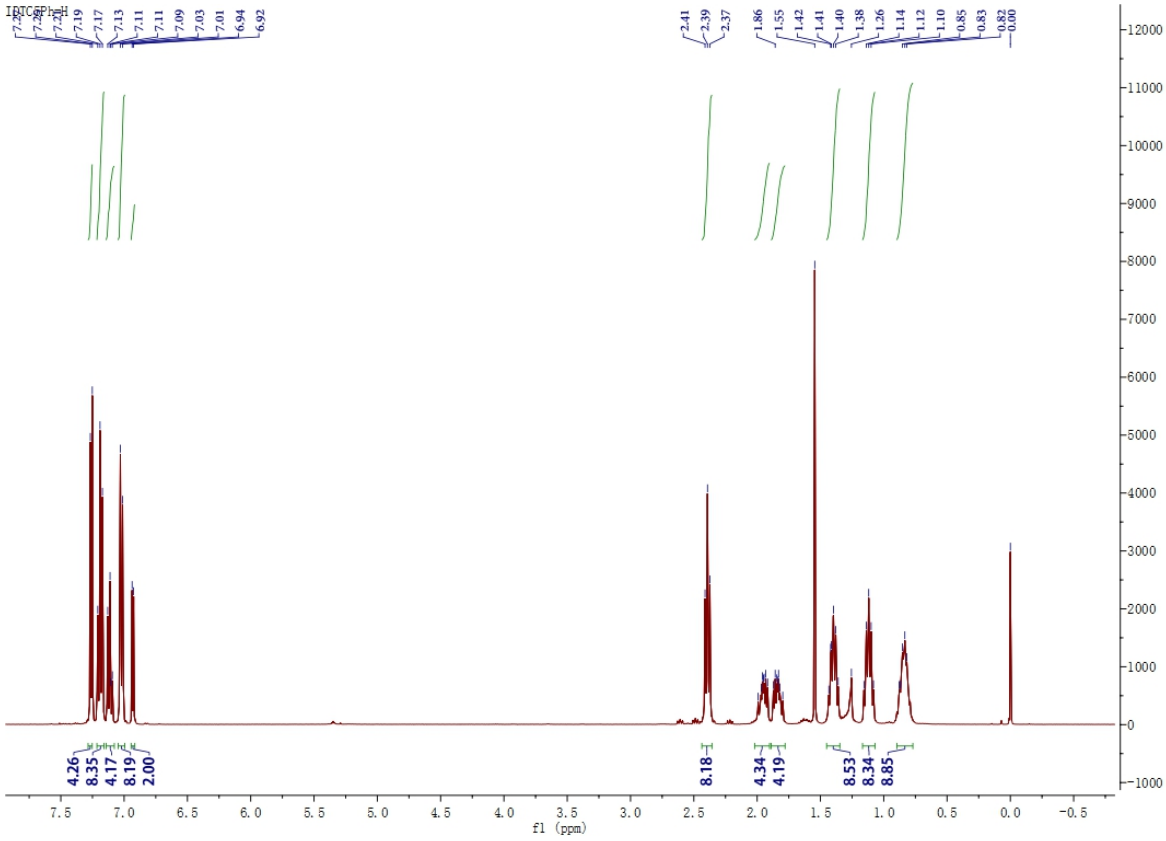

The ^{1}H NMR spectrum of IDTC5Ph.

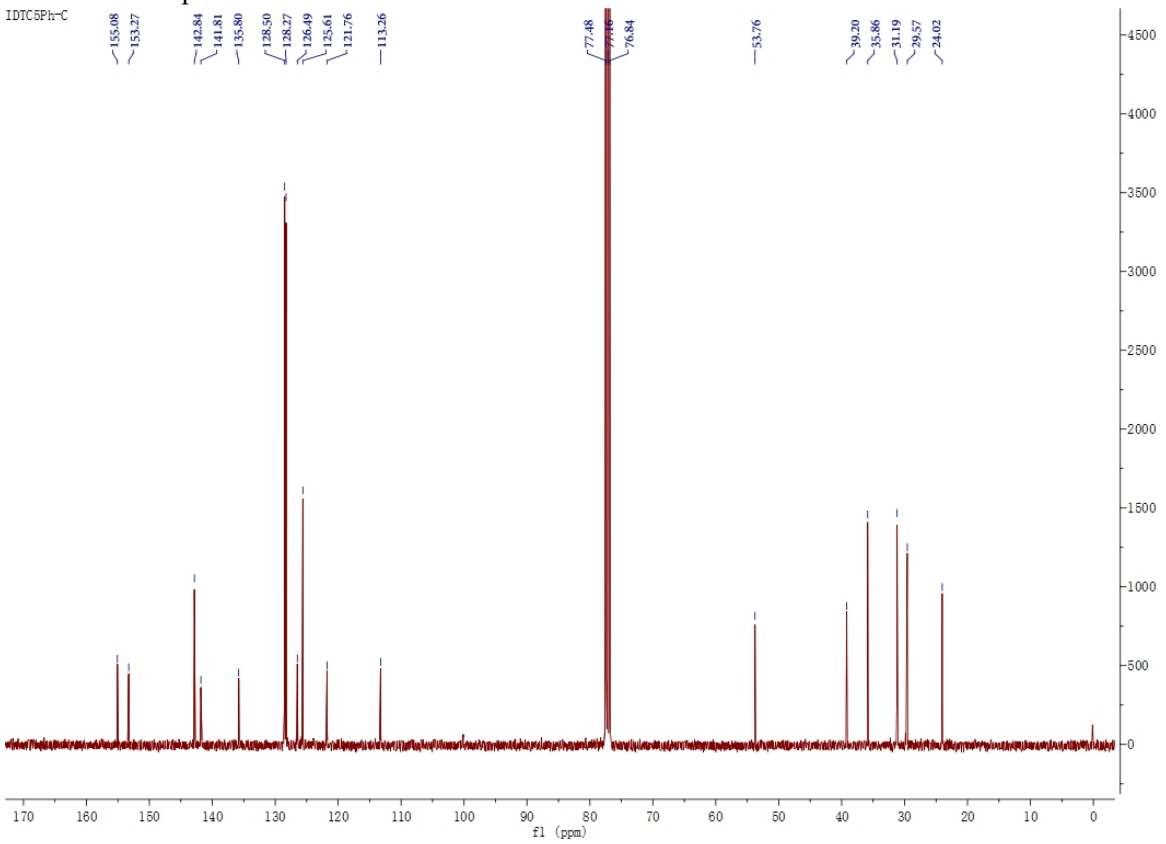

The ^{13}C NMR spectrum of IDTC5Ph.

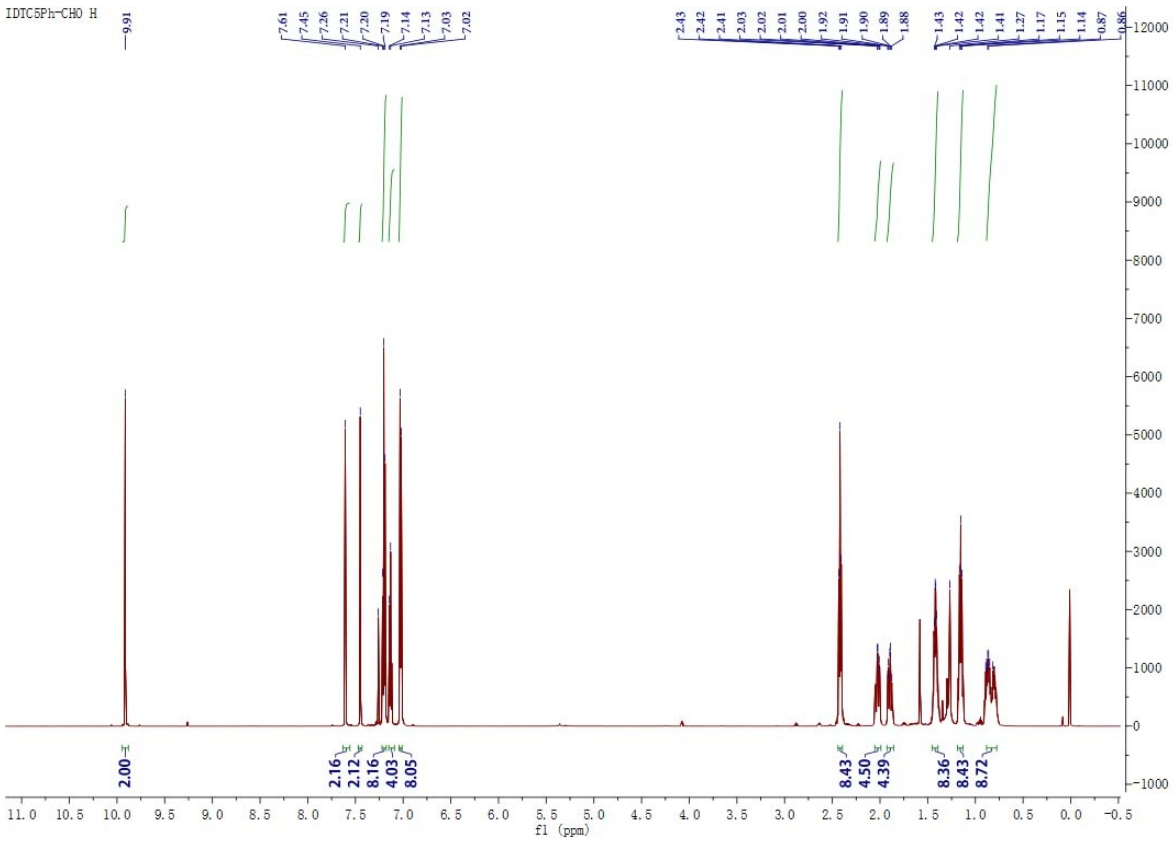

The ^{1}H NMR spectrum of IDTC5Ph-CHO.

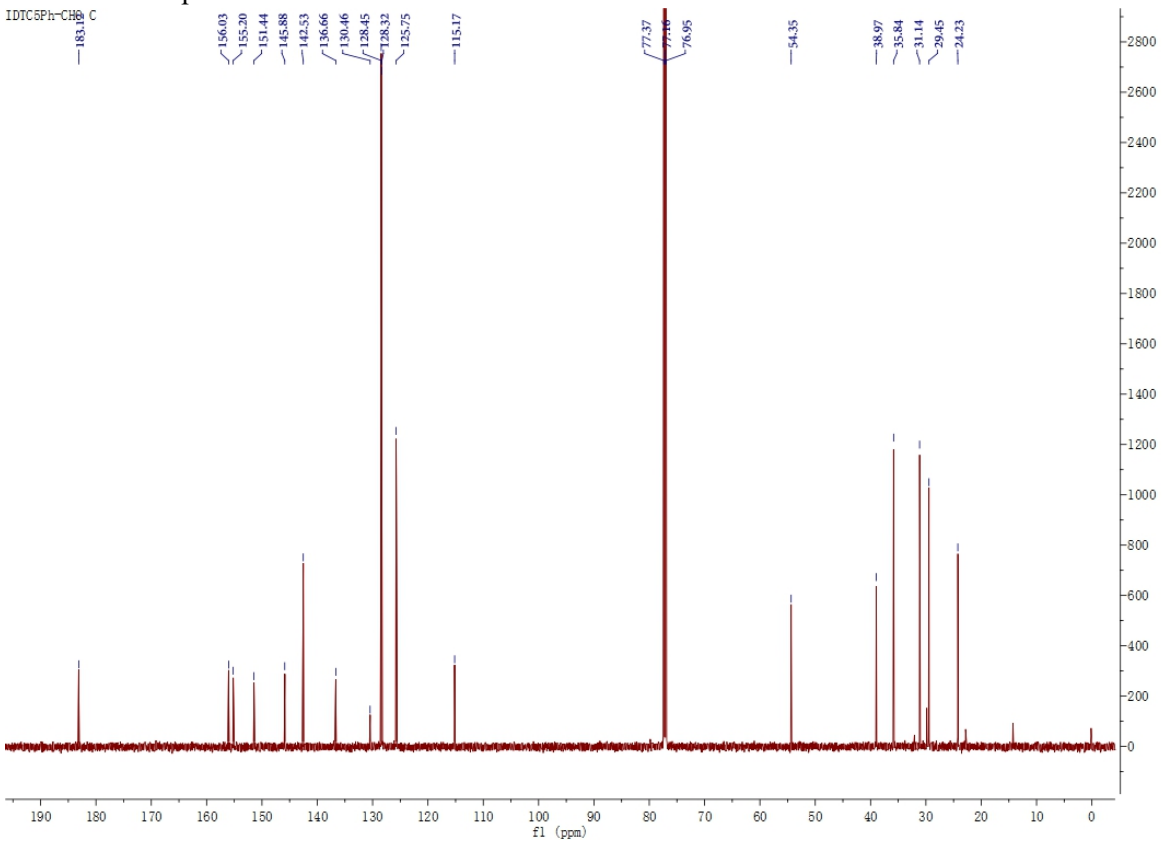

The ^{13}C NMR spectrum of IDTC5Ph-CHO.

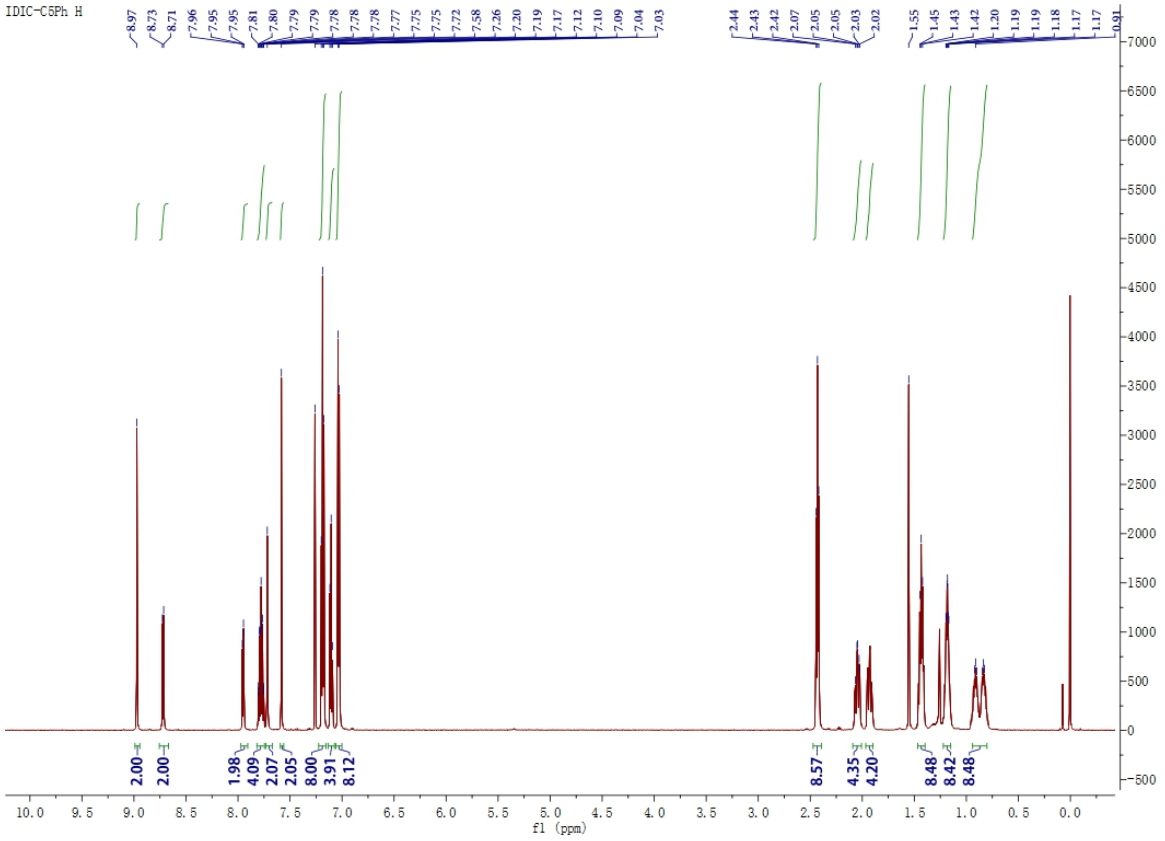

The ^{1}H NMR spectrum of IDIC-C5Ph.

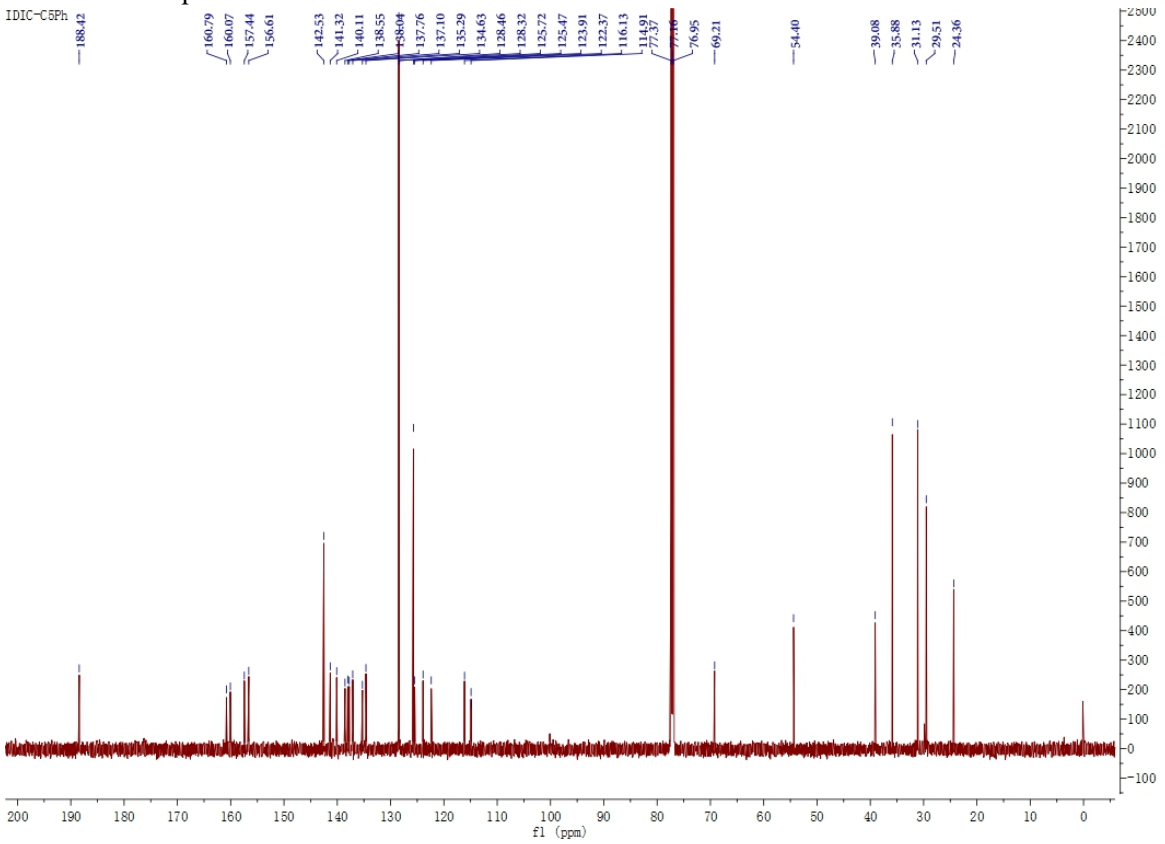

The ^{13}C NMR spectrum of IDIC-C5Ph.

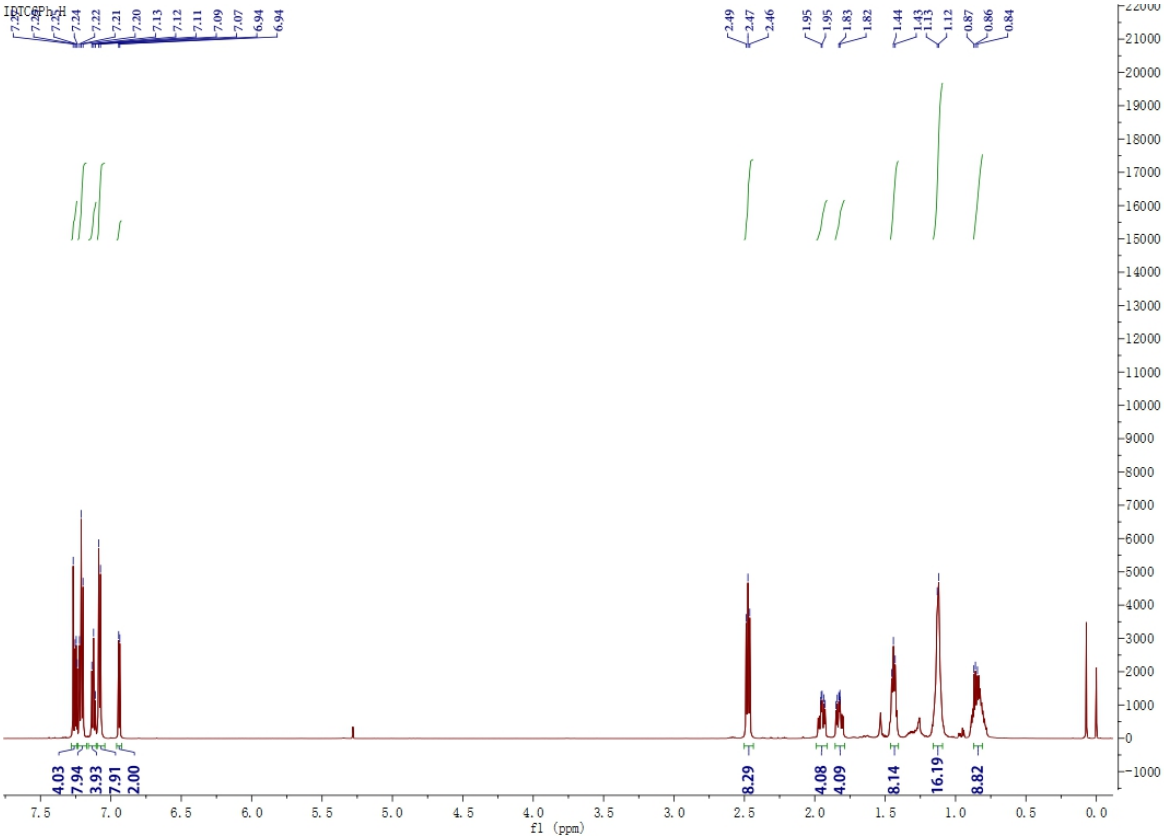

The ^{1}H NMR spectrum of IDTC6Ph.

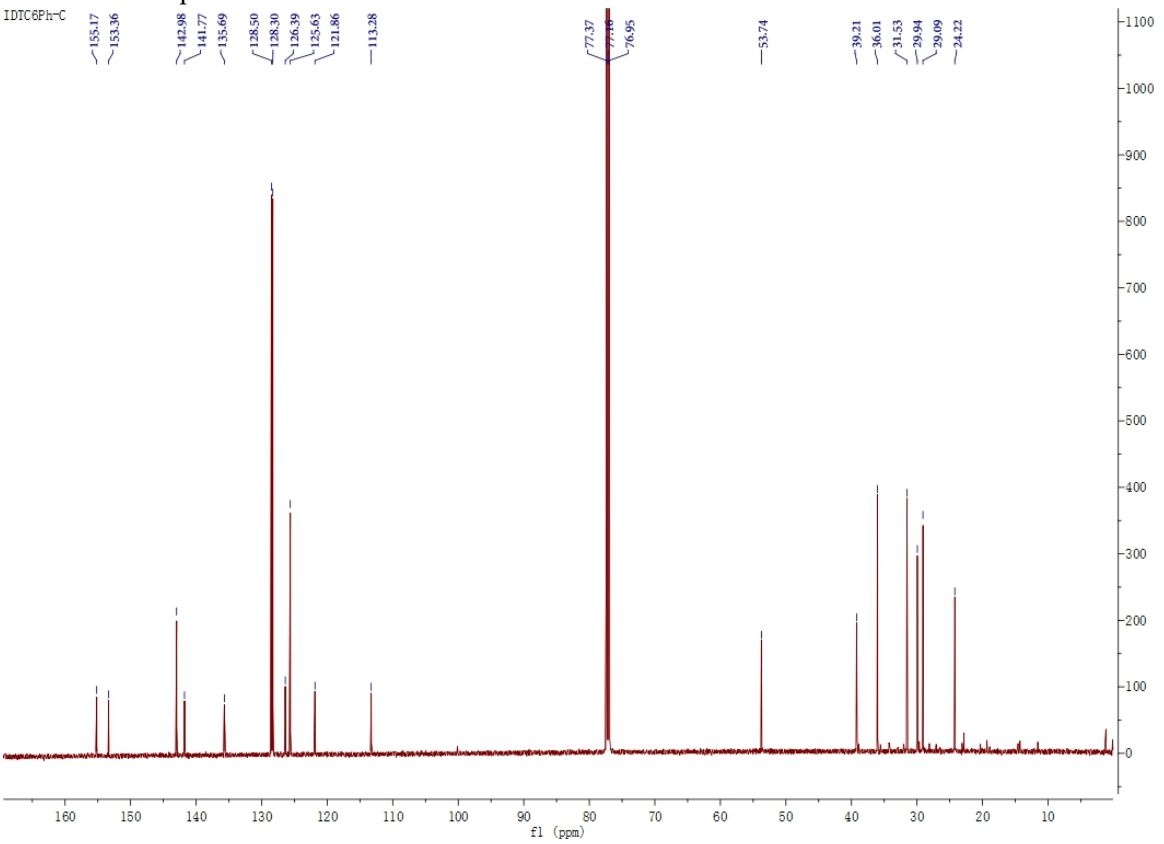

The ^{13}C NMR spectrum of IDTC6Ph.

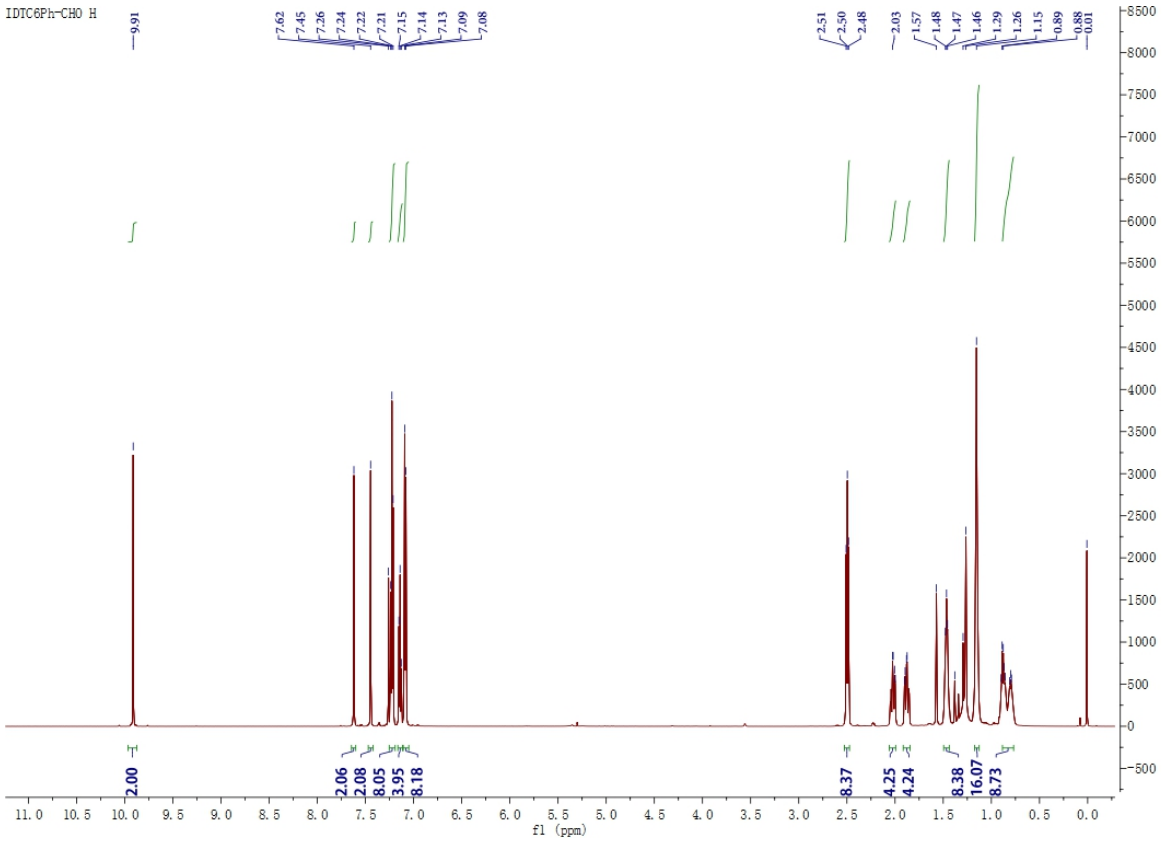

The ^{1}H NMR spectrum of IDTC6Ph-CHO.

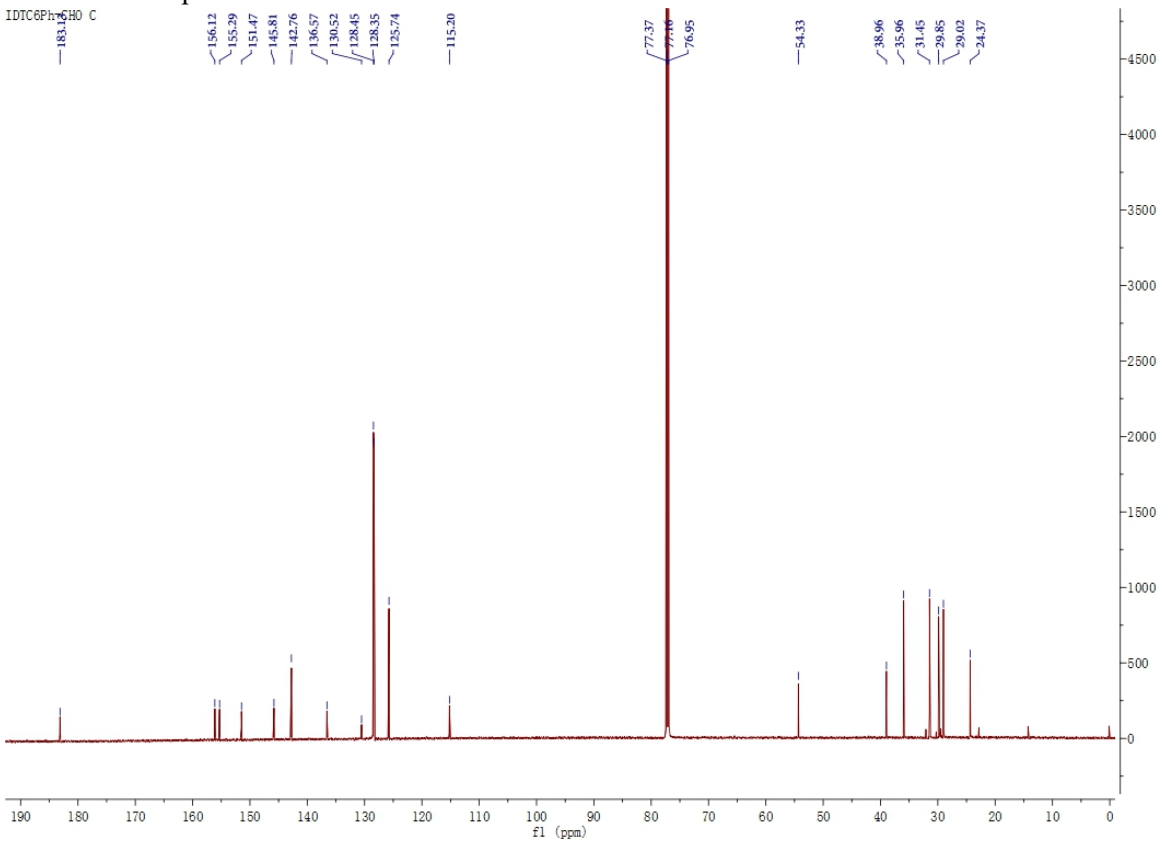

The ^{13}C NMR spectrum of IDTC6Ph-CHO.

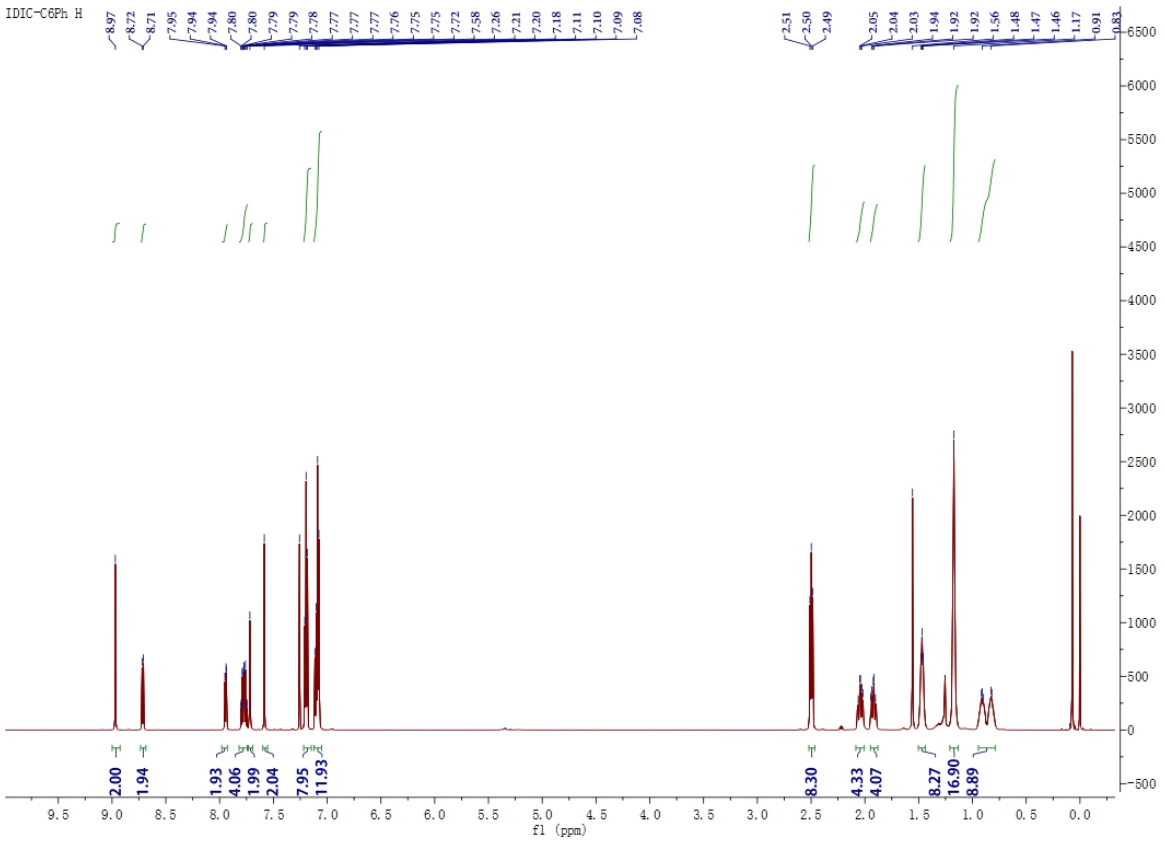

The ^{1}H NMR spectrum of IDIC-C6Ph.

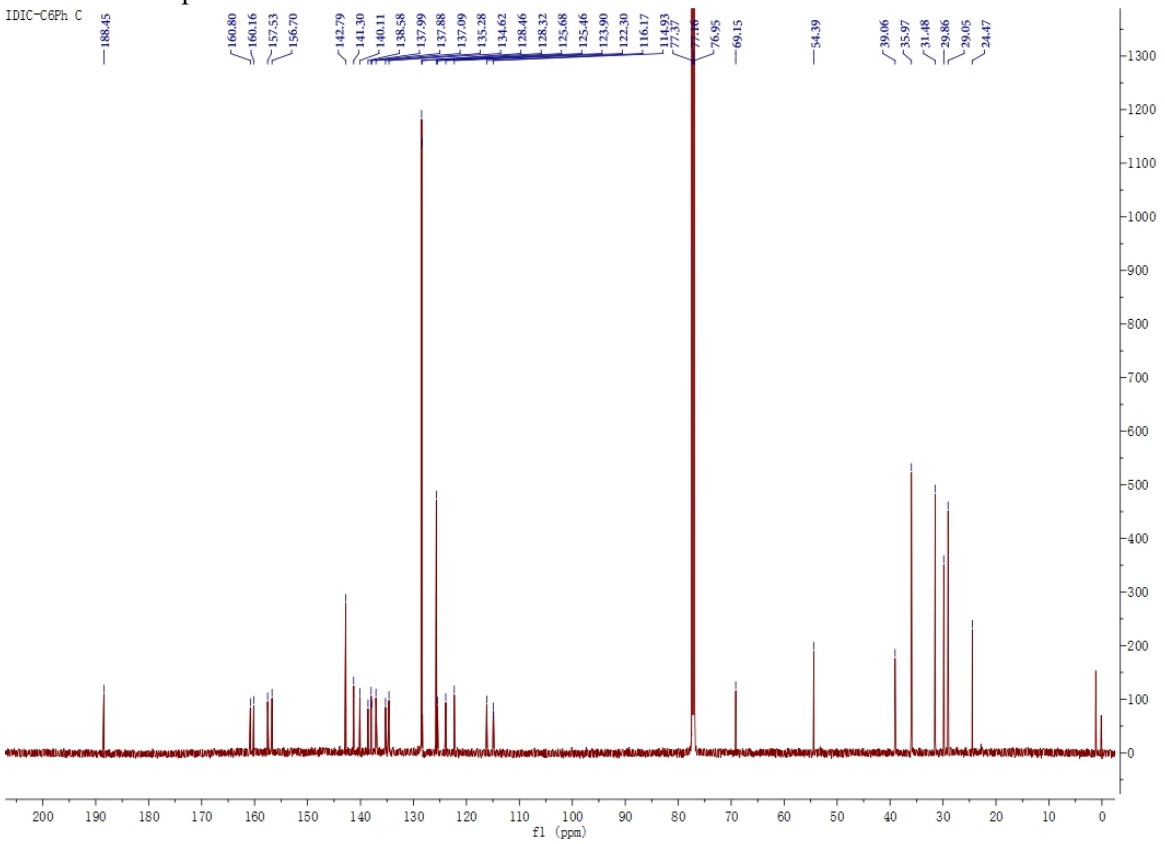

The ^{13}C NMR spectrum of IDIC-C6Ph.

References:

S1 Gao, W., An, Q., Hao, M., et al. (2020). Thick‐film organic solar cells achieving over 11% efficiency

and nearly 70% fill factor at thickness over 400 nm. Adv. Funct. Mater. ***30***, 1908336.

S2 Feng, S., Zhang, C., Liu, Y., et al. (2017). Fused-ring acceptors with asymmetric side chains for high-performance thick-film organic solar cells. Adv. Mater. ***29***. 1703527.

S3 Li, S., Ye, L., Zhao, W., et al. (2017). Design of a new small-molecule electron acceptor enables efficient polymer solar cells with high fill factor. Adv. Mater. ***29***. 1704051.

S4 Sun, C., Pan, F., Bin, H., et al. (2018). A low cost and high performance polymer donor material for polymer solar cells. Nat. Commun. ***9***, 743.

S5 Luo, Z., Sun, C., Chen, S., et al. (2018). Side-chain impact on molecular orientation of organic semiconductor acceptors: high performance nonfullerene polymer solar cells with thick active layer over 400 nm. Adv. Energy Mater. ***8***, 1800856.

S6 Yang, Y., Zhang, Z.G., Bin, H., et al. (2016). Side-chain isomerization on an n-type organic semiconductor itic acceptor makes 11.77% high efficiency polymer solar cells. J. Am. Chem. Soc. ***138***, 15011-15018.

S7 Lee, S., Park, K.H., Lee, J.H., et al. (2019). Achieving thickness‐insensitive morphology of the photoactive layer for printable organic photovoltaic cells via side chain engineering in nonfullerene acceptors. Adv. Energy Mater. ***9***, 1900044.

S8 Yuan, J., Zhang, Y., Zhou, L., et al. (2019). Single-junction organic solar cell with over 15% efficiency using fused-ring acceptor with electron-deficient core. Joule ***3***, 1140-1151.

S9 Liu, Y., Zhao, J., Li, Z., et al. (2014). Aggregation and morphology control enables multiple cases of high-efficiency polymer solar cells. Nat. Commun. ***5***, 5293.

S10 Nguyen, T.L., Choi, H., Ko, S.J., et al. (2014). Semi-crystalline photovoltaic polymers with efficiency exceeding 9% in a ~300 nm thick conventional single-cell device. Energy Environ. Sci. ***7***, 3040-3051..

S11 Choi, H., Ko, S.J., Kim, T., et al. (2015). Small-bandgap polymer solar cells with unprecedented short-circuit current density and high fill factor. Adv. Mater. ***27***, 3318-3324.

S12 Sun, K., Xiao, Z., Lu, S., et al. (2015). A molecular nematic liquid crystalline material for high-performance organic photovoltaics. Nat. Commun. ***6***, 6013.